AFOSR-TR-97

REPORT DOCUMENTATION PAGE

0275

1. AGENCY USE ONLY (Leave blank)	2. REPORT DATE	3. REPORT TYPE AND DATES COVERED
	04/08/97	Final Technical Report 10/21/93 - 10/31/96

4. TITLE AND SUBTITLE	5. FUNDING NUMBERS
MICRO-OPTO-MECHANICAL SYSTEMS	F49620-94-C-0007

6. AUTHOR(S)

Dr. Kaigham J. Gabriel

7. PERFORMING ORGANIZATION NAME(S) AND ADDRESS(ES)	8. PERFORMING ORGANIZATION REPORT NUMBER
Case Western Reserve University 10900 Euclid Avenue Cleveland, OH 44106-7221	

9. SPONSORING/MONITORING AGENCY NAME(S) AND ADDRESS(ES)	10. SPONSORING/MONITORING AGENCY REPORT NUMBER
AFOSR/NA 110 Duncan Avenue, Suite B 115 Bolling AFB, DC 20332-8050	

11. SUPPLEMENTARY NOTES

19970616 142

12a. DISTRIBUTION AVAILABILITY STATEMENT	12b. DISTRIBUTION CODE
Approved for public release; distribution unlimited.	

DTIC QUALITY INSPECTED 2

13. ABSTRACT (Maximum 200 words)

We have finished a three-year university/industry cooperative program for basic research and technology development in the area of micro-opto-mechanical systems (MOMS). The impetus ofr this work came from the results of our research on microactuators as well as a review of other current research. Our program addressed two components: (i) the development of basic micro-opto-mechanical devices which can be combined in to complex MOMS; and (ii) the development of the basic processes necessary for the fabrication of these devices.

The ultimate goal of this project was the development Micro-Opto-Mechanical Systems (MOMS) which integrate the coordinated motions of basic microactuators, passive/active optical components, microsensors, and microelectronics in order to realize complete pre-assembled optical systems that can be mass produced at low unit cost. Such micro-fabricated MOMS: (i) do not need component alignment; (ii) can be mass produced (i.e., should be on the order of dollars per unit device); (iii) have high packing density; (iV) can be directly integrated with electronics; and (v) should be low-power, small and light weight.

We used microactuator technology to develop a family of basic micro-opto-mechanical devices which can be utilized indivuidually or in combination to fabricate miniature optical scanners for a variety of applications, optical interconnect switches andf requency-controlled laser diodes for telecommunications and computers as examples which we have completed in this program.

14. SUBJECT TERMS			15. NUMBER OF PAGES
			38
			16. PRICE CODE

17. SECURITY CLASSIFICATION OF REPORT	18. SECURITY CLASSIFICATION OF THIS PAGE	19. SECURITY CLASSIFICATION OF ABSTRACT	20. LIMITATION OF ABSTRACT
Unclassified	Unclassified	Unclassified	

MICRO-OPTO-MECHANICAL SYSTEMS

Final Report

Covering the Period

October 21, 1993 to October 31, 1996

Contract No.
FQ8671-9301675

Electronic Systems Technology Office
Advanced Research Projects Agency
Department of Defense
Attention: Dr. Kaigham J. Gabriel

by

Case Western Reserve University
Cleveland, Ohio 44106-7221

PROJECT SUMMARY

We have finished a three-year university/industry cooperative program for basic research and technology development in the area of micro-opto-mechanical systems (MOMS). The impetus for this work came from the results of our research on microactuators as well as a review of other current research. Our program addressed two components: (i) the development of basic micro-opto-mechanical devices which can be combined into complex MOMS; and (ii) the development of the basic processes necessary for the fabrication of these devices.

The ultimate goal of this project was the development Micro-Opto-Mechanical Systems (MOMS) which integrate the coordinated motions of basic microactuators, passive/active optical components, microsensors, and microelectronics in order to realize complete pre-assembled optical systems that can be mass produced at low unit cost. Such micro-fabricated MOMS: (i) do not need component alignment; (ii) can be mass produced (i.e., should be on the order of dollars per unit device); (iii) have high packing density; (iv) can be directly integrated with electronics; and (v) should be low-power, small, and light weight.

We used microactuator technology to develop a family of basic micro-opto-mechanical devices which can be utilized individually or in combination to fabricate miniature optical scanners for a variety of applications, optical interconnect switches and frequency-controlled laser diodes for telecommunications and computers as examples which we have completed in this program.

In our original proposal we identified the following basic micro-opto-mechnaical devices which individually or in combination could be used for many optical system applications. These basic devices were:

- microlenses and waveguides — lenses and waveguides micromachined from SiO_xN_y films deposited with graded index of refraction
- beam splitters — simple pellicle-type structures micromachined from SiO_xN_y films deposited with constant index of refraction
- (rotary) micromotor polygon scanner — a rotating, tall (e.g., greater than 50 μm) reflector
- cantilever scanner — a tilting, tall (e.g., greater than 50 μm) reflector
- lens on a linear translator — a microlens on a lateral-resonant-type microactuator
- reflector on a linear translator — a tall reflector on a lateral-resonant-type microactuator
- (rotary) micromotor chopper/shutter — a simple micromotor with alternating optically transmitting/opaque rotor segments
- waveguide on a deformable bridge — an optical waveguide fabricated on a bimetallic bridge microactuator
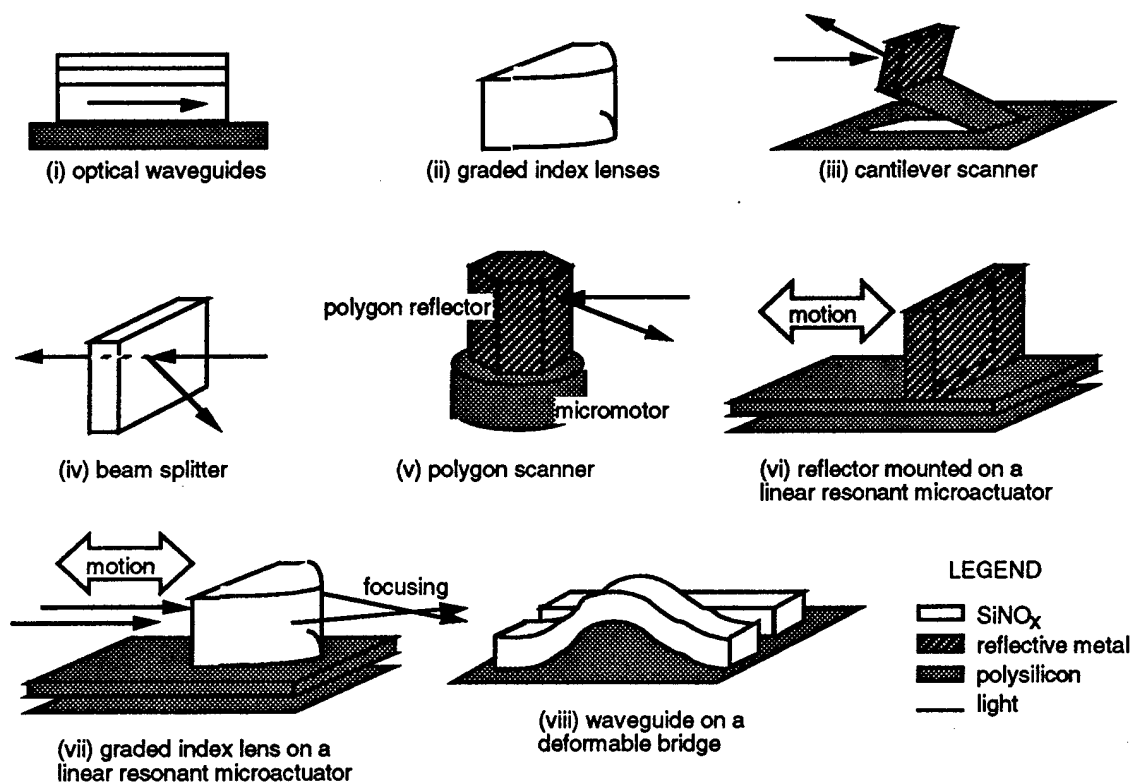
Figure 1. A set of basic MOM devices.

(i) optical waveguides   (ii) graded index lenses   (iii) cantilever scanner

(iv) beam splitter   (v) polygon scanner   (vi) reflector mounted on a linear resonant microactuator

polygon reflector   micromotor

motion   focusing

(vii) graded index lens on a linear resonant microactuator

(viii) waveguide on a deformable bridge

LEGEND

SiNO$_x$
reflective metal
polysilicon
light

To this original set we have added diffraction gratings. A primary objective of our work was optical scanners. The approach which we have concentrated upon in this program was a diffraction grating mounted on a rotating micromotor.

In the area of optical telecommunications, we worked with our industrial partner, Reliance Electric and their Comm-Tech Division, to identify MOMS critical to practical implementation of optic fiber subscriber loops. One factor that has emerged is that all applications require the development of some form of optical microbench that will permit the low-cost manufacture of pre-aligned, hybrid optical fiber systems. Our first device was a twelve-fiber vee-groove splice for optical ribbon cables. This device was designed and fabricated at Case, and tested to AT&T specifications by Reliance Electric. Our second project was optical rib waveguides for the eventual integration of microfabricated receptacles for optical fibers, laser diodes, and photodiodes with optical waveguides and directional couplers.

To develop MOMS, we established the basic fabrication processes required for the program: polysilicon surface micromachining for the mechanical devices and high-aspect-ratio microfabrication of metallic microstructures for the reflective surfaces. Our MOMS fabrication approach has been to: first fabricate

all mechanical components using polysilicon surface micromachining; then carry out the fabrication of the reflective surfaces in a one-mask step. This partitioned fabrication approach is practical since each fabrication process is used to implement specific mechanical and optical components of the MOMS. Additionally, the processing requirements are easily met.

We have developed two polysilicon surface micromachining processes centered around the fabrication of micromotors. We use a simple (e.g., 3 mask) process in which individual micromotors can be fabricated rather quickly and with low processing complexity. This process and the associated micromotors was used for rapid prototyping in basic studies for improving and characterizing micromotor performance [1]. We used a second process which incorporates sufficient flexibility (e.g., 7–10 masks) for a broad range of micromotor designs, sizes, and interconnections. These polysilicon surface micromachining processes were also be used for other (e.g., lateral-resonant and parallelogram types) electric microactuators required in our work.

We used an in-house thick-resist and plating process for rapid prototyping of our MOMS requiring tall (e.g., 20 μm or greater) reflective metallic microstructures with nearly vertical walls. This process is needed for producing optical elements such as translatable reflectors, as well as for micromechanical devices such as microrelays. This high aspect ration electroless nickel plating process was successfully used to produce high current (approximately 100 mA) capacity microrelays.

Finally, we developed a process for fabricating optical waveguides which can be integrated with our procedures for polysilicon surface micromachining and nickel surface micromachining on the same substrate. gratings. This was demonstrated by successfully produced all-silicon optical waveguides on (110) silicon substrates in which we etched fiber guiding U-grooves.

In device development, we have fabricated basic micro-optical devices such as translatable reflectors, rotating mirrors and diffraction gratings, optical waveguide couplers, scanning optical mirrors, and diffraction gratings. We developed optical microbenches, optical switches, and frequency-controlled laser diodes for optical telecommunications applications in cooperation with our industrial partner. A critical need in optical telecommunications is that of a low-cost, mass-produced frequency stabilized laser diode sources which we have demonstrated using a (111) beam on a (110) substrates which was electrostatically deflected to tune the frequency of a diode laser.

A primary objective of our program was optical scanning. We have produced micromotor optical scanners which use diffraction grating elements on the micromotor rotors to scan optical beams.

As we developed our MOM devices and systems, we have been conducting detailed studies of micromotor operational reliability with emphasis on stiction, dynamic friction, and wear. We are also conducting detailed optical characterization of fabricated micro-optical components such as diffraction gratings all-silicon waveguides. We are conducting detailed characterization of our drive and control electronics, the electromechanical performance of our MOM devices and systems, and the electrical performance of microfabricated relays. We have developed new control algorithms and control electronics suitable for integration with a polysilicon micromotor and believe that integration of these control schemes and control electronics with the rotating diffraction grating we have previously developed could lead to a commercial optical microscanner with applications ranging from optical switches to bar code readers.

Conclusions

We have demonstrated a MOMS based laser beam scanner bar code reader using a diffraction element micromotor scanner in the laboratory. Single and pyramidal diffraction elements have been fabricated on the polished rotors of polysilicon surface micromachined, large-area micromotors and evaluated. The scanner micromotors had solid polysilicon rotors with diameters in the range of 0.5 to 2 mm, with 1 and 2 µm rotor/stator gaps, and with both salient-pole and wobble designs.

To produce a usable microscanner we have developed various processing techniques for the micromotor fabrication. A CMP process was developed and characterized for polysilicon surface micromachining. It provided a method of global planarization and reduced the polysilicon surface roughness to values comparable to virgin single-crystal silicon. The reduced surface roughness provided by CMP enhanced feature definition and delineation in polysilicon significantly improving the optical performance of diffraction elements fabricated on polysilicon by reducing optical scattering. High-quality diffraction beam profiles indicated that polished polysilicon is a viable material for production of low-cost, high-quality microscanners.

The fabricated diffraction elements were tested at visible wavelengths and were verified to have spatial periods closely matching their design. Stepping and continuous mode dynamic performance of the microscanner was demonstrated with visible diffraction orders at meter distances away. Continuous mode operation was found to be more suitable for high-speed, high-resolution, scanning applications. Self-assembled monolayers were found to significantly improve the scanner micromotors' reliability and overall dynamic performance characteristics. In fact, it was not possible to produce usable microscanners without such SAM films

Nickel Surface Micromachining

A surface micromachining process, which we call nickel surface micromachining, has been developed for the fabrication of metallic electrostatic microactuators [3, 4]. This process uses a nickel structural layer which is directly deposited on the polysilicon sacrificial layer by electroless nickel plating without the need for a metallic seed layer. This process can be used with high-aspect-ratio photolithography to produce lateral resonant translational devices with nickel plated sidewalls which can be used to produce linearly translatable microreflectors or electrical microrelays [4]. The process consists of our steps: (i) deposition of electrical isolation and sacrificial layers; (ii) fabrication of the plating mold; (iii) deposition of the nickel by electroless plating; and (iv) release of the plated devices. This process can be described in detail as:

i) deposition of isolation and sacrificial layers
Starting with a (100) silicon wafer, a 0.5μm to 1μm thick oxide layer is thermally grown at 950°C. This oxide layer is used for electrical isolation of the substrate and also protects the substrate during the initial device release step in KOH. Next, a 2.5 μm to 5 μm thick undoped polysilicon layer is deposited at 600°C by LPCVD. This polysilicon film acts as a plating and sacrificial layer for the subsequent electroless plating of nickel microstructures. The thickness of the polysilicon has been shown to affect the surface roughness of the subsequently plated nickel film, with thicker polysilicon films resulting in nickel films with larger values of surface roughness.

ii) fabrication of the plating mold
For the plating mold features defined in photoresist, large height-width aspect ratios, vertical sidewalls, and material compatibility with plating chemicals are desirable. To meet these objectives, we have developed and used a high-aspect ratio photolithography process to produce features as small as 2 μm in 20 μm thick photoresist with steep sidewalls [5].

iii) deposition of nickel by electroless plating
Prior to plating, the polysilicon surface to be plated is pretreated by an acid etch, followed by a 2-3 minute deposition of palladium as a starting catalyst, and a final acid etch to remove any tin oxide. This pretreatment causes the polysilicon surface to become porous, providing mechanical bonding sites for adhesion of the nickel to the polysilicon. The etch rate and surface morphology of polysilicon vary depending upon the polysilicon grain size which, in turn, depends upon the LPCVD deposition conditions. Very short etch times do not uniformly initiate the nickel plating; long etch times reduce the polysilicon film thickness significantly, reducing the mechanical integrity of the nickel film.

<u>iv) release</u>
The etched devices are released by selectively etching the polysilicon layer from everywhere but the anchor regions under the plated nickel. We use a timed etch of the polysilicon using 40 wt.% KOH at approximately 6 μm/hour.

We have also developed a high-aspect ratio photolithography process using a positive photoresist of high viscosity and high transparency, and standard UV light exposure [5]. In this process, the wafers undergo a dehydration bake and HMDS (hexamethyldisilazine) vapor prime in a HMDS oven at 150°C. A thick photoresist (Hoechst, AZ 4620) is then spin-coated at 2000 rpm. Edge bead removal is performed to ensure a smooth photoresist surface. The wafers are then pre-baked at 95-100°C for 30 minutes in a convection oven. The wafers undergo an additional coating, edge bead removal, and pre-bake under the same conditions to give a photoresist layer that is approximately 20 μm thick. The wafers are then aligned using a contact aligner with a standard UV light source. The plating molds are formed after development in an alkaline developer (Hoechst, AZ-400K) diluted in de-ionized water.

Photoresist is usually postbaked after exposure to improve both adhesion of the photoresist to the substrate and chemical resistance of the photoresist. By removing this postbake and the consequent high temperature mold distortions, we were able to achieve mask features as small as 2 μm in 20 μm thick photoresist with steep side walls.

The surface characteristics of the plated nickel and the polysilicon layer were investigated using mechanical test microstructures. Passive T-structures deformed upon release due to the residual tensile stress in the film. From measurement of these deformations and knowledge of device geometry, the average residual stress was determined to be 89 Mpa. Lateral resonant devices with folded beam suspensions, to relieve stress, were resonated by electrical excitation. From the resonant frequencies and device geometries, the average Young's modulus of these electroless nickel films was determined to be 154 GPa.

Lateral Translational Reflectors

As an extension of the previous work on nickel surface micromachining, we also developed a lateral translating reflector using the same basic processing as was previously used for a rotating polygon scanner [6,7]. A three-mask design for the linear translatable reflector was developed, and our nickel plating process was used to fabricate the device shown in Figure 2. We have obtained released nickel plated features with lengths of 500μm and 20μm thickness. The nickel films were deposited in a state of very low tensile stress [8]. The nickel microactuator devices are currently undergoing detailed mechanical testing.

Such translational mirrors can be used in interferometers and/or for tuning laser diodes.
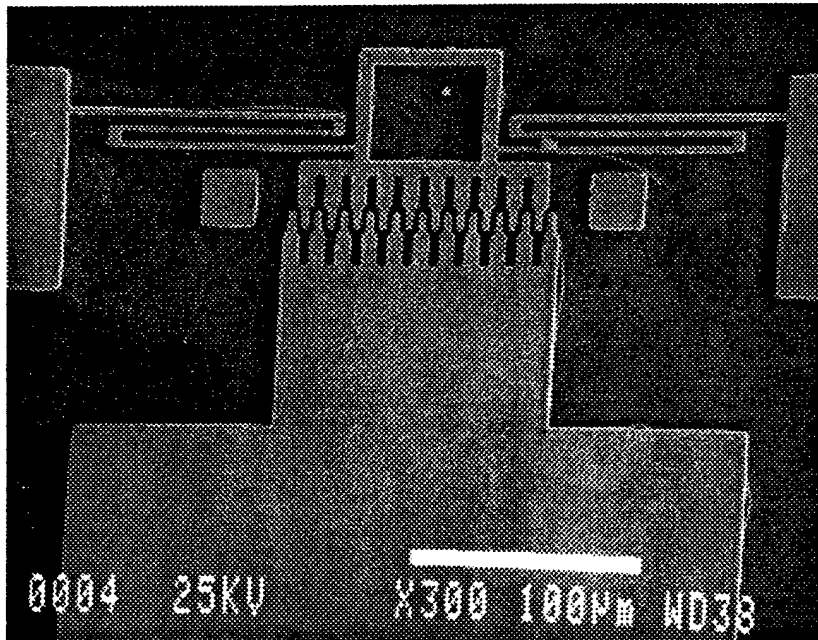

Figure 2. Electrostatic drive lateral translational reflector. Note that the sidewall of the surface at the top center of the image is nickel plated and can be used as an optical reflector.
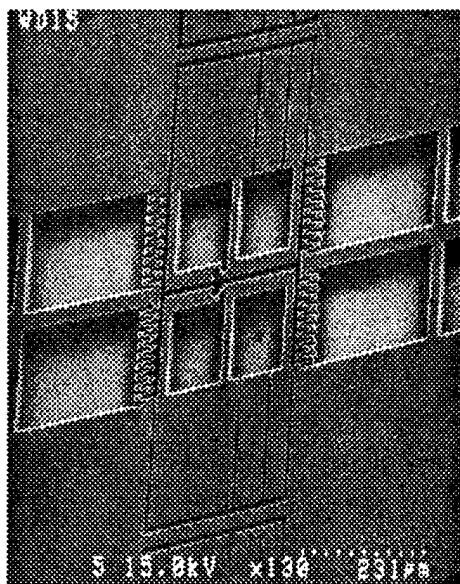
Microrelays

Electrostatic micro-relays have been designed and fabricated as a specific application of nickel surface micromachining [9,10]. Experimental tests of these devices have revealed low contact resistance (on the order of ohms) for current loads up to few hundred mA. Switching times of these microrelays were in the range of a few milliseconds. The devices are based on comb-finger structure designs where electrostatic actuation is used for lateral motion of contacts to close and open the microrelay. Preliminary electrical measurements have been taken to determine the switching and contact characteristics.

Figures 3 shows a photoresist mold for a typical microrelay device fabricated using the nickel surface micromachining process. Figure 4 shows an actual fabricated microrelay. The comb drive on the right is used to actuate the relay and close the contact. Once the relay actuation voltage is switched off, the elastic restoration forces in the suspension beams force it to open. The comb drive on the left would be used to generate an additional restoration force to overcome any stiction that may occur at the relay contact. The contact region of the microrelay is designed such that the stiffness of the suspension prevents the electrostatic attraction force, between the signal pads and the relay contact, from closing the relay. Additionally, the design allows for rubbing action between the relay contact and signal pads to scratch off any native oxide that may be present on the metal surfaces upon closing. The relay operation is governed by the force, F_s, on the relay contact due to the signal voltage, V_s, and the restoring force, F_r, in the suspension. The ratio F_s/F_r should be as small as possible to prevent the signal voltage from closing the relay. Typical calculated restoration forces for nickel surface-micromachined relays with suspension beam lengths and widths of 150 μm and 3.5 μm, respectively, are at least 10 μN. Therefore, with "worst-case" parameters, the ratio F_s/F_r is at least 0.001, ensuring that the signal voltage does not close the microrelay.

The fabricated nickel microrelays have operated consistently for ~10^3 cycles for actuation voltages of approximately 200V. This relatively high actuation voltage was required to overcome the large stiffness of the suspensions, attributed to the non-rectangular nature of the photolithography process and fabrication process aberrations. Since 200V was the limit of our driving power supply, it was not clear whether reliable actuation could be achieved by even higher voltages for more cycles of operation.

The resonant frequencies were measured by driving the microrelays with a function generator and varying the frequency until the amplitude of the vibration reached a maximum (determined visually under the probe station microscope). Resonant frequencies ranged from 5–40 kHz, depending upon
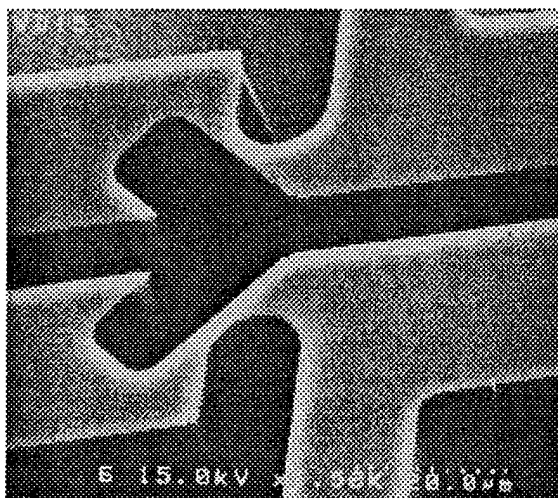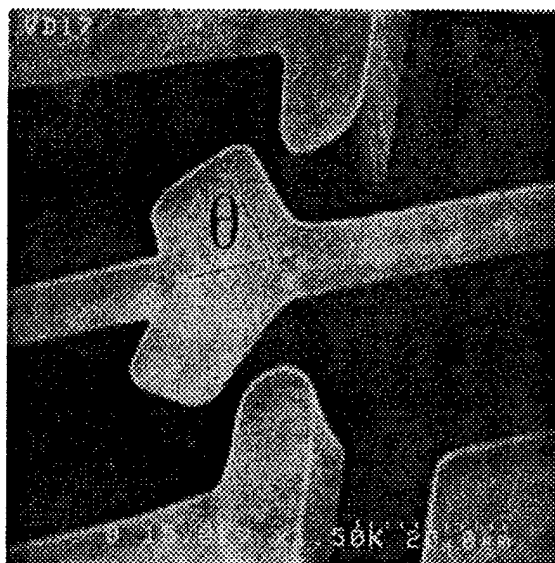
(a)
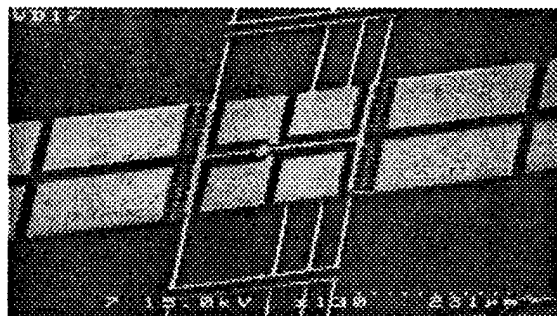
(b)

Figure 3. SEM photographs showing (a) a 20 μm-thick plating microrelay mold pattern formed by high-aspect-ratio lithography, and (b) final 16 μm-thick electroless plated nickel microrelay showing a folded-beam suspension with 3.5 μm wide and 150 μm long beams.

(a)

(b)

Figure 4. SEM photographs showing (a) a 20 μm-thick plating microrelay mold pattern formed by high-aspect-ratio lithography: (a) overview of microrelay mold pattern; and (b) close-up of a θ=60° microrelay contact and signal pads.

Figure 5. Oscilloscope display showing typical microrelay operation at 1 kHz for 200V actuation. The switched signal is 5V.

the device geometry and film thickness. However, consistent microrelay operation was observed only for driving frequencies of 1 kHz or less.

Figure 5 shows a typical 15 μm-thick microrelay being driven at 1 kHz, switching a 5V signal across the contacts. Only a portion of the switched signal is displayed due to the sampling limitations of the oscilloscope; nevertheless, the periodic nature of the microrelay action is clear. The contact travel from equilibrium position was 2 μm. From the graph, the switching frequency was determined to be 1 kHz. The measured current through the microrelay was 100 mA. The apparent contact area is no larger than 5 μm by 15 μm, based on the contact geometry design and the nickel film thickness. However, the actual contact area is smaller due to the non-rectangular cross-sections of the contact and signal pads, as well as the curved shape of the signal pads. The current density through the contact is therefore at least 1.3 mA/μm^2. The total resistance across the contacts of a closed microrelay was approximately 30Ω, leading to a contact resistance value of 15Ω per contact. The driving voltage provided an actuation force of 100 μN while contact travel required 80 μN. Consequently, a contact pressure of at least 0.27 MPa was achieved.

No degradation of the relay contacts was observed visually for microrelay current density less than 2 mA/μm^2 through the contacts. For current densities up to 6 mA/μm^2, the nickel contact regions changed color from yellow to light orange, implying some level of degradation. When the microrelay contact current density was greater than 6 mA/μm^2, the relay contacts melted.

Microscanners

In the area of microscanners, we have developed new optical microscanners which incorporate diffraction gratings on the rotor of electrostatic polysilicon micromotors as shown in Figure 6. The diffraction gratings were produced by chemical etching, then chemical-mechanically polished (CMP) to reduce the average surface roughness to less than 17Å, consequently improving the optical efficiency of the gratings.
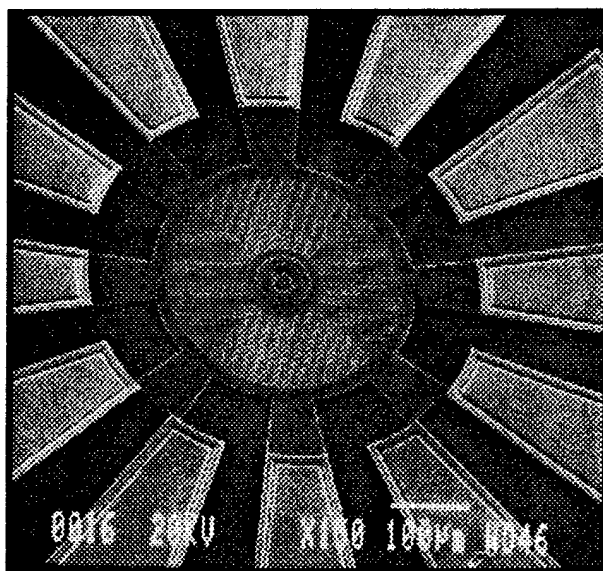

Figure 6. SEM photo of a rotating diffraction grating microscanner. The motor is a 500-μm diameter salient-pole side-drive micromotor with polished rotor/stator polysilicon and pyramidal grating element of 1.8 μm period.

Our approach to microscanners has been to integrate electrostatic polysilicon micromotors with optical elements. We have produced polysilicon surface micromachining using a simple (e.g., 3 mask) process in which individual micromotors can be fabricated rather quickly and with low processing complexity [6]. We have designed and fabricated flange bearing millimeter-sized wobble and salient-pole micromotors using this three-mask process. These are the largest side-drive, polysilicon surface micromachined electrostatic motors reported to date. Typical dimensions for these scanners are rotor diameters of 0.5 to 1.0 mm, rotor/stator gaps of 1.5 to 2.5 μm and rotor/stator thicknesses of 5 μm. In the past twelve months, we have used the three mask process to produce planar microscanners consisting of a polygon reflector rotated by an electrostatic micromotor [11, 12]. Polysilicon surface micromachining was used to fabricate the micromotor and high-aspect-ratio microfabrication of metallic microstructures was used to fabricate the reflective surfaces.

We have used a five mask process which is an extension of the three mask process to produce diffraction grating microscanners similar to that shown in

Figure 6 [13]. These devices require thick (e.g., 5.5 μm) polysilicon rotor/stator films to provide sufficient mechanical stiffness and to prevent out-of-plane warping of large area rotors. However, with increasing LPCVD polysilicon thickness, the film roughness increases. Longer diffusion times are also needed to subsequently dope the polysilicon, further increasing the surface roughness. This inherent polysilicon surface roughness results in two limitations: (i) feature size definition and quality degradation; and (ii) undesirable optical scattering.
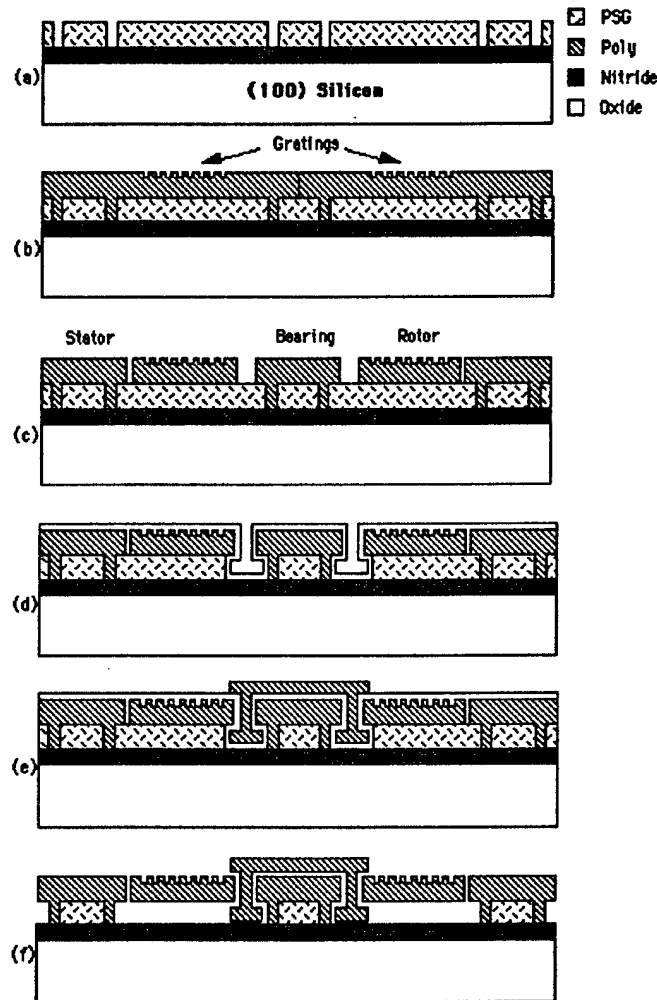
Figure 7. Cross-sectional schematics describing the microscanner fabrication process: (a) after anchor definition and patterning; (b) grating definition and patterning; (c) rotor/stator definition and patterning; (d) bearing clearance oxidation; (e) bearing definition and patterning; and (f) released device.

The fabrication of diffraction gratings requires that an average surface roughness (R_a) less than 20Å as well as stringent line width and spacing control during photolithography and pattern delineation to obtain satisfactory optical performance. To meet these requirements, we have used chemical-

mechanical polishing (CMP) to polish the surface of the polysilicon micromotor rotors on which the gratings are fabricated. With CMP, the average polysilicon surface roughness (R_a) of our 5.5 µm-thick polysilicon films on which the gratings are fabricated was reduced from 420Å to below 17Å (with less than 1500 Å film removal). Figure 8 demonstrates the significant feature size definition and quality (e.g., sidewall smoothness) improvement, as well as the substantial surface roughness reduction, achieved with CMP. To produce a diffraction grating on the rotor of the micromotor, the gratings are patterned and etched (~0.5 µm deep) into the polysilicon layer using an isotropic dry etch in order to approximate a sinusoidal grating profile for high optical diffraction efficiency [15]. Next, the rotor/stator pattern is defined and delineated using a highly anisotropic dry etch to produce 1 µm rotor/stator gaps. The flange mold is then defined and etched, followed by a 0.3 µm bearing clearance oxidation. A 1.2 µm-thick polysilicon layer is deposited by LPCVD and patterned to produce the bearing.

(a)   (b)
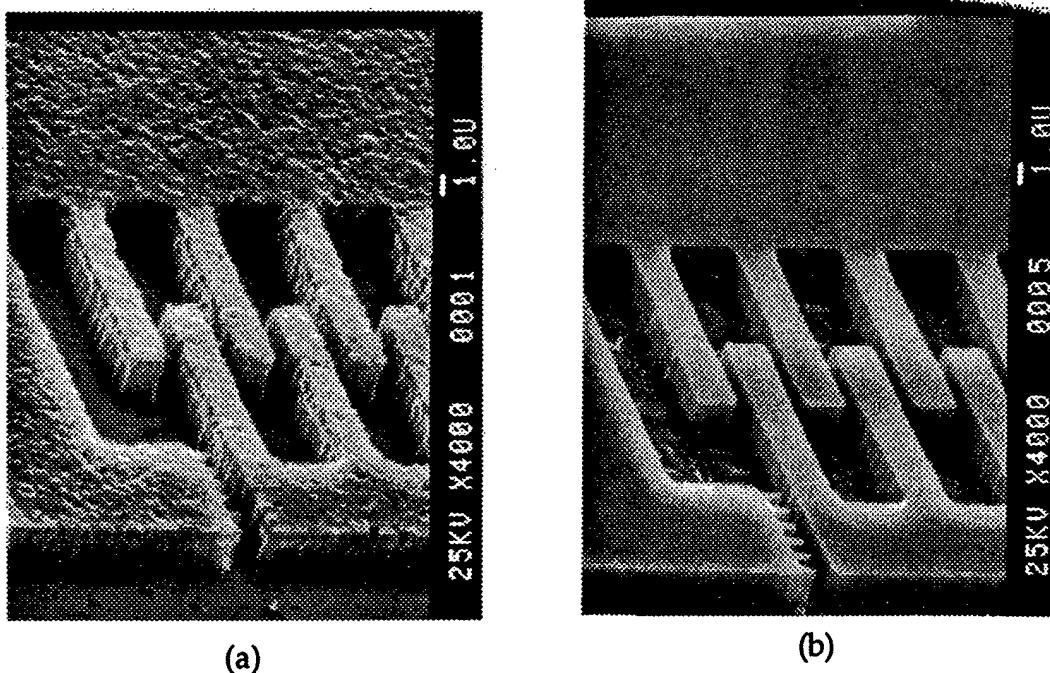
Figure 8. Close-up view of polysilicon comb fingers fabricated in (a) unpolished and (b) polished 3.5µm-thick polysilicon. Note the improved feature definition, side wall quality, and line width resolution, as well as polysilicon surface roughness.

In the area of microscanners, we have been working on improving the reliability and lifetime of released devices. We have developed a matrix of process parameters to optimize the performance of diffraction grating microscanners. We have been developing control algorithms and electronics for the microscanner. The drive waveforms have a significant impact upon the rotation of the motor. In particular, scan applications such as bar code reading require constant velocity of the optical beam which can be

-13-

accomplished by overlapping the drive phases. On the other hand, optical switches simply require stepping operation of the micromotor with suitable settling of the micromotor to its final position. We have met with our industrial partner and have defined specifications for a commercial micromotor grating optical scanner.

Our current device fabrication is based on a five mask process which is an extension of the three-mask process described in [1]. Appendix 1 outlines the process traveler for current microscanner fabrication. Initially, 4500Å of LPCVD silicon nitride for electrical insulation, followed by 3.5 μm of PSG for a sacrificial layer, are deposited. The stator and the bearing post anchors are then patterned, followed by a 5.5 μm-thick rotor/stator LPCVD polysilicon deposition. Thick (e.g., 5.5 μm) polysilicon rotor/stator films has been used in our designs to provide mechanical stiffness and to prevent out-of-plane warping of large area rotors due to polysilicon residual stresses. This may not have been the best design approach. With increasing LPCVD polysilicon thickness, the film roughness increases due to increased grain size. Longer diffusion times were also needed to subsequently dope the polysilicon by thermal diffusion, further increasing the surface roughness.

	Undoped		Doped	
Before CMP	580Å		517Å	
After CMP	17Å		19Å	
Total Removal	2000Å		3591Å	
Oxidation Temperature	900°C	1100°C	900°C	1100°C
After 45 minutes Oxidation	19Å	134Å	51Å	114Å
After 345 minutes Oxidation	34Å	216Å	78Å	221Å

Table 1. Average roughness (Ra) for 11 μm-thick polysilicon films, before and after CMP, as well as subsequent to thermal processing of polished films.

This inherent polysilicon surface roughness resulted in two limitations: (1) feature size definition and quality degradation; and (2) undesirable optical scattering. Thermal processing causes polysilicon grain growth, resulting in increased surface roughness which is detrimental to producing etched diffraction gratings. Several groups of wafers were evaluated to quantify these effects. Polished heavily-phosphorous-doped and undoped 11 μm-thick films were oxidized in steam for 45 minutes and 345 minutes at temperatures of 900°C and 1100°C. The 345 minute oxidation at 1100°C is the 1.5 μm-thick oxidation recipe used. Subsequent to polysilicon deposition and doping, surface roughness measurements were taken before CMP, after CMP, and after the oxidation processes. The results, shown in Table 1, verify that thermal processing has an adverse effect on surface smoothness.

Increasing oxidation time and temperature increases the resulting surface roughness. It has been suggested that the increase in surface roughness at higher temperatures is due to the decrease in the dominant texture (e.g., {110}), and the increase of other orientations with a slightly increased rate of grain growth due to recrystalization [14]. It was observed that doped films processed at 900°C resulted in films with a higher roughness value than undoped films. It has been suggested that, as dopants in polysilicon films are increased, the grain-boundary mobility of polysilicon increases as large amounts of phosphorous are segregated at the grain boundaries. This increase in grain-boundary mobility facilitates the grain growth and results in higher surface roughness [14]. The data indicates however that doping effects do not dominate the process at 1100°C, as seen by comparing the doped and undoped roughness data in Table 1. Reference [14] gives an explanation for this phenomenon based on the different solid solubility of the dopants at different oxidation temperatures and the resulting enhanced grain boundary oxidation.

Figures 9 and 10 show SEM photographs of typical diffraction grating salient-pole and wobble microscanners, respectively. Although it is not clear from these SEMs the micromotor scanners exhibit high definition mechanical features and incorporate high quality sinusoidal diffraction gratings.

(a)   (b)
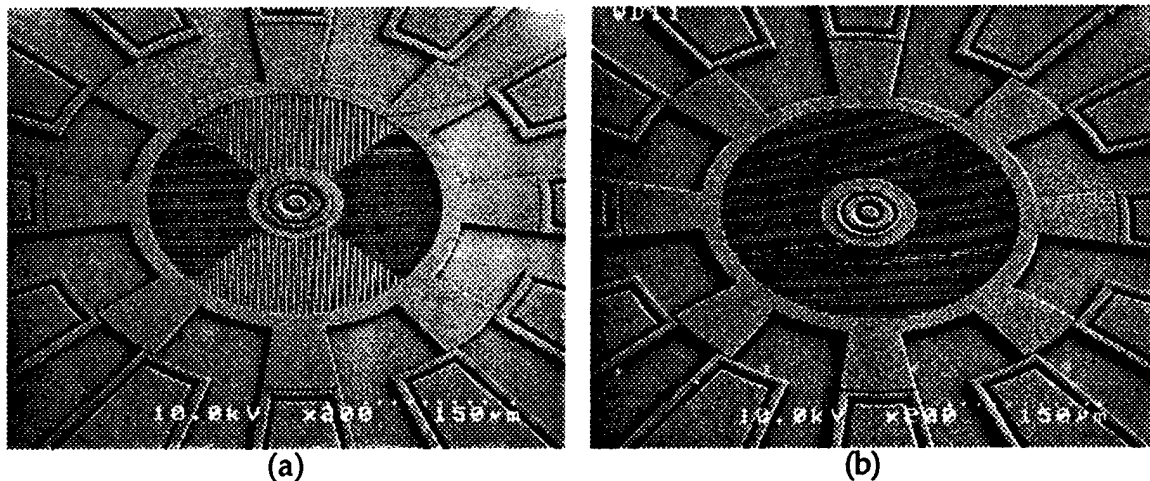
Figure 9. Typical 500 µm-diameter, salient-pole, microscanners with polished rotor/stator polysilicon: (a) pyramidal grating element of 3.86 µm period; and (b) single grating element of 3.86 µm period.

<p style="text-align:center">(a)   (b)</p>
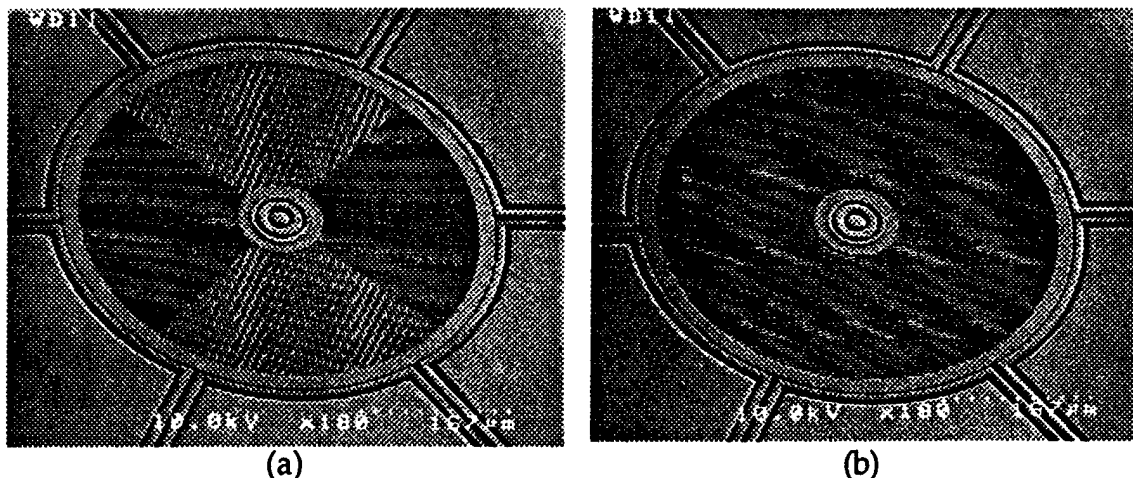
Figure 10. Typical 500 μm-diameter, wobble, microscanners with polished rotor/stator polysilicon: (a) pyramidal grating element of 3.86 μm period; and (b) single grating element of 3.86 μm period.

Mechanical Problems and Issues

We have produced micromotor scanners with rotor diameters from 0.5 m m to 2.0 mm using the previously described processing. Upon normal release in 49 % (by weight) HF of salient-pole microscanners, it was observed that all rotors would stick to the substrate. Super-critical Carbon Dioxide (CO_2) release was needed to prevent stiction to the substrate after release [16]. It was observed that the motors produced as described above could be released without stiction and displaced upon mechanical probing, but none was electrically operational. Only the 0.5 mm-diameter motors responded with a limited vibration upon electrical excitation.

Initially, it was observed that all motors larger than 0.5 mm-diameter had all their rotor blades bowed and touching the substrate even with super-critical CO_2 release. Only the 0.5 mm-diameter motors had some of their rotor blades (one or two out of eight) flat. It was determined that the residual stress variation through the thickness in the 5.5 μm-thick structural polysilicon was relatively high with 0.7 μm of bowing towards the substrate associated with every 100 μm of feature length [17]. Given that the rotors were solid disks with no stress relief features (as the designs reported in [12]), annealing of the scanner micromotor was needed to relieve the residual stresses of the polysilicon. Different combinations of annealing time and temperature were investigated, with satisfactory annealing occurring at 900°C for about 4 days, or at 1100°C for 45 minutes. Only the 0.5 mm diameter motors benefited from annealing with their rotor blades becoming flat. These 0.5 mm rotor diameter motors operated smoothly in room air, but required mechanical probing to start. It is hypothesized that the reason these motors required probing was due to the increased frictional torque at the bearing. Bearing frictional torque increases with increasing bearing radius (i.e., the lever arm of the bearing friction force), especially for the salient-pole micromotors in which the

<p style="text-align:center">-16-</p>

bearing operation results in sliding contacts . The 0.5 mm-diameter motors reported in [12] utilized bearing radii in the range of 10 to 18 μm for reliable operation. All bearing radii for our present micromotor scanners are 25 μm, thus the frictional torque associated with them is larger than those reported in [12] for the same rotor diameter and film thickness.

Self-assembled monolayers (SAM) have been reported to improve the performance of polysilicon micromotors [18]. After coating the 0.5 mm rotor diameter scanner micromotors with OTS (C_{18}) SAM, spontaneous operation of the motors upon electrical excitation was achieved. Furthermore, the SAM coating of the motors eliminated the need for super-critical CO_2 release as stiction was reduced substantially due to the hydrophobic nature of the OTS coating. Without the super-critical CO_2 release and the SAM coating, the annealed motors might work (upon mechanical probing) for a while, but their operation was sporadic and non-repeatable. Furthermore, these motors returned to sticking to the substrate after storage. It was observed that high humidity had an adverse effect on the operation of the scanner micromotors with humidity above 46% resulting in erratic motor operation. Micromotors utilizing the SAM coating were reversible to reliable operation in low humidity environments whereas those without the SAM coating were not.

Upon addressing the above mentioned issues, the micromotor scanners operated smoothly and reproducibly in room air for operational durations as long as eight continuous hours (~150,000 cycles). The motors have shown stable and repeatable operation over an eight week testing period. It is believed that the micromotor scanner reliability and life time can be greatly improved in future designs by addressing many of the above mentioned issues at the design and fabrication stages, e.g., the bearing radius can be designed to be smaller (e.g., 10 μm-diameter) to reduce the frictional torque using a slightly modified anchoring scheme and rotors may be designed with stress relief features while maintaining large enough areas to accommodate the gratings.

Micromotor Performance Characteristics
Both 1 and 2 μm rotor/stator gap scanner micromotors were operational. Minimum operating voltages were as low as 15V and 45V for wobble and salient-pole scanner micromotor designs, respectively. The maximum rotor speeds were 7 rpm and 5200 rpm for wobble and salient-pole motor designs, respectively. Figure 11 shows typical step transient data for 500 μm-diameter, 2 μm rotor/stator gap salient-pole scanner micromotors with and without OTS coating. The rise time of the step response for the motor coated with OTS is shorter than that without OTS. This result indicates that the motor with OTS coating experiences less friction (in agreement with the results reported in [18]). Figure 12 shows gear ratio as a function of excitation voltage for 500 μm-diameter, 2 μm rotor/stator gap wobble scanner micromotor with and without OTS coating. The gear ratio for the scanner micromotors coated

with OTS is close to the ideal gear ratio and is smaller than that without OTS. This implies that OTS reduces slip in wobble scanner micromotors as reported in [18].
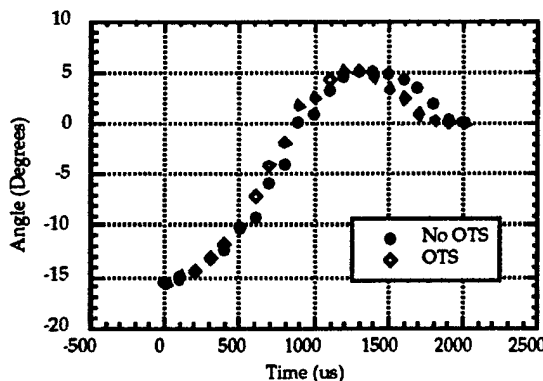

Figure 11. Step transient data for 500 μm-diameter, 2 μm-gap, salient-pole scanner micromotor with and without OTS coating.

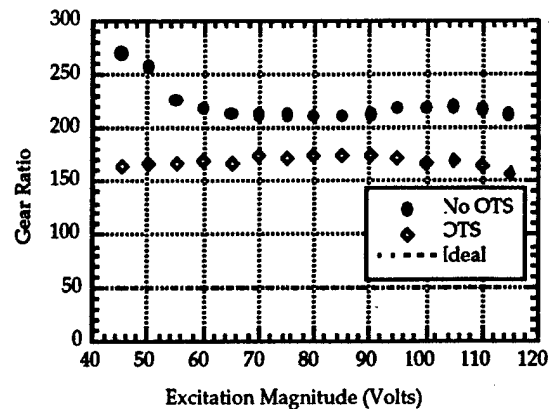Figure 12. Gear ratio as a function of excitation voltage for 500 μm-diameter, 2 μm-gap wobble scanner micromotor with and without OTS coating.

Static Optical Performance

The optical properties of reflective diffraction gratings fabricated on polished and unpolished polysilicon rotors demonstrate the importance of polishing the rough polysilicon surface for optical applications. Figure 5 shows that CMP reduced the undesirable light scattering due to the excessive polysilicon surface roughness to values comparable to that achieved for gratings on single crystal silicon wafers. (For comparison, gratings were etched into single crystal silicon wafers, in addition to polished and unpolished polysilicon surfaces). The grating periods for the nominally 2 and 4 μm gratings were measured to be 1.80 μm and 3.86 μm, respectively. This result is in close correspondence with the target design and the difference was attributed to variations in timed etching and photolithography.
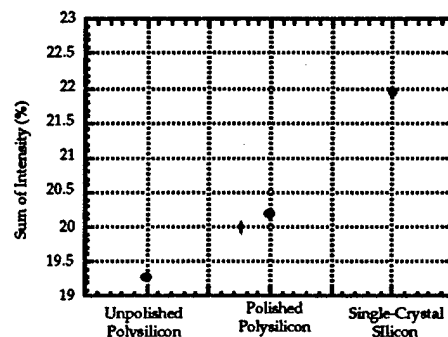
Figure 13. Sum of intensity from all diffraction orders from gratings fabricated on polished and unpolished polysilicon, as well as single-crystal silicon wafers.

Characterization of the diffracted laser beam profiles with a CCD camera indicated that at distances on the order of one meter from the microscanner

-18-

all diffraction orders provided gaussian beam profiles, with gratings on polished polysilicon producing a higher degree of spatial uniformity and lower beam divergence than those on unpolished polysilicon. Figure 13 compares measured beam profiles, with gratings on polished polysilicon at a distance of 0.5 m from the wafer. The measured diffraction orders for 1.80 μm gratings were separated by $20.79°\pm0.62°$ and those for the 3.86 μm gratings by $9.8°\pm0.53°$. The line width and diffraction angles were uniform for similar gratings on the same wafer and between different wafers. Optical scanning at distances up to several meters without external optics was readily possible and demonstrated. The effects of small (0.5 mm diameter) motor size and extraneous motor features (i.e., 25 μm radius bearing) was found to be negligible upon the overall optical performance of the microscanner.

Dynamic Optical Performance

Scanning operation was tested using a laser beam incident on the microscanner. Multiple diffraction orders were visible at meter distances. The scanned beams were examined with a silicon photodiode and a digital oscilloscope. The uniformity of the scanned beams was measured over many revolutions of the microscanner. Figure 14 shows a typical intensity profile for a salient-pole microscanner during stepping operation. As a reference, a trace of a signal synchronous to the excitation voltage of the scanner micromotor is superimposed. In stepping mode operation, the next phase in the micromotor excitation signal is triggered after the rotor aligns with the stator pole. The scanner micromotor was also run using the continuous mode micromotor controller reported in [12]. This controller uses a pulse overlap scheme with a pulse width that is the same duration as the step transient rise time, such that the next phase in the excitation sequence is triggered before the rotor aligns and the initially excited phase is grounded. This results in the rotor being drawn to the next stator phase in the excitation sequence without reducing the speed or reversing directions. Figure 15 shows typical scans obtained from scanner micromotors operated in stepping and continuous modes. Continuous mode operation is more suitable for optical scanning and is being used in the bar code scanning application.
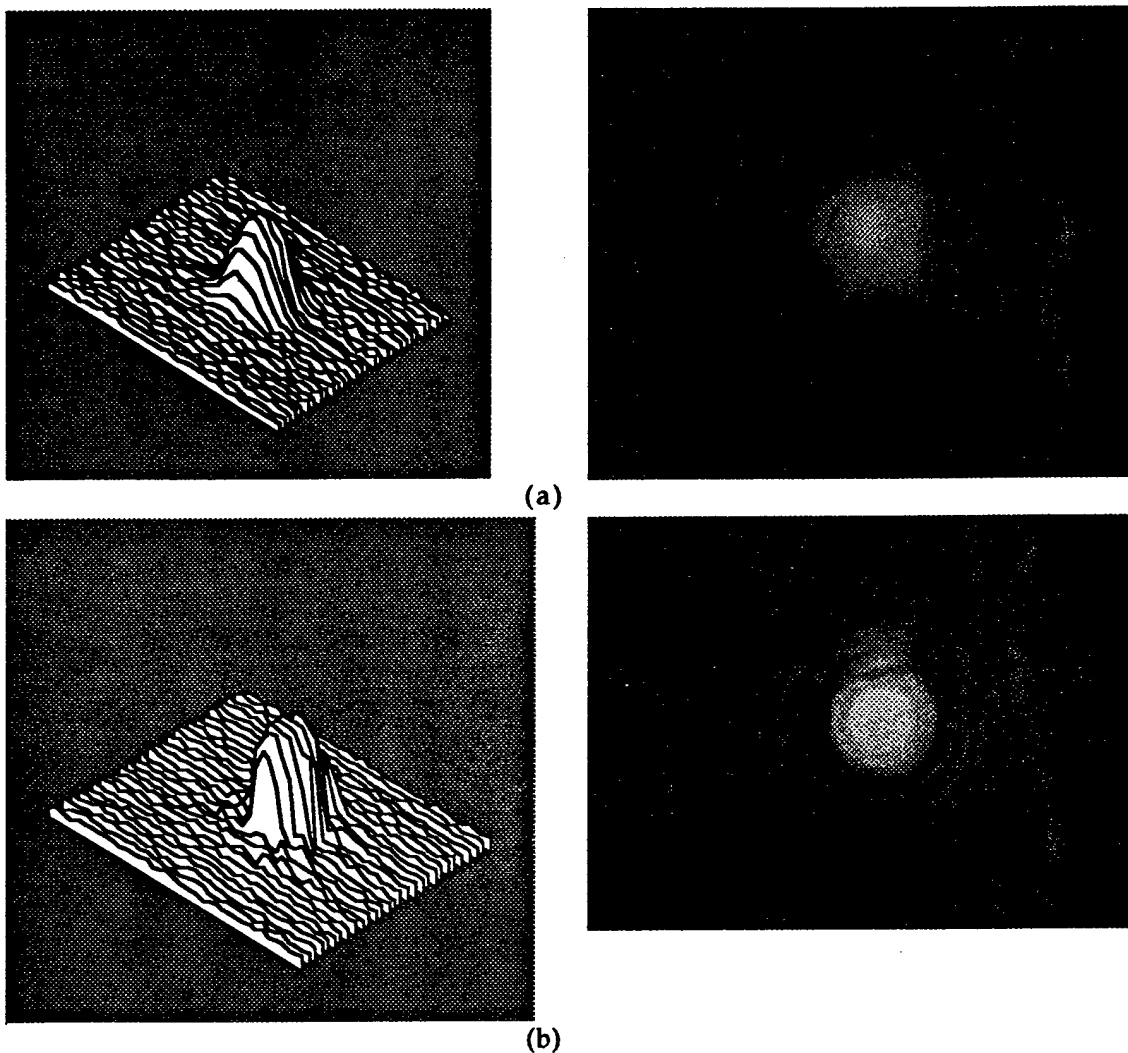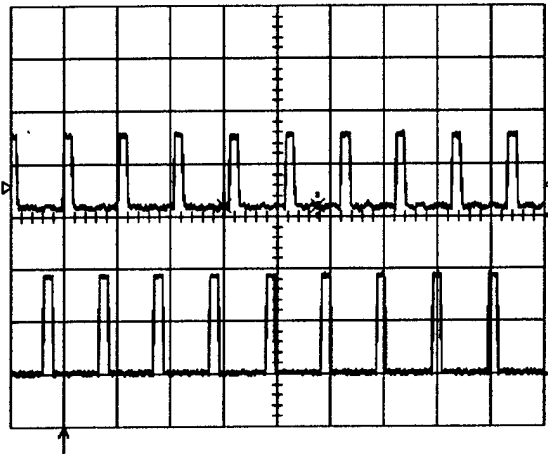
Figure 14. Beam intensity profiles (left) and spot quality (right) from similar gratings fabricated on (a) unpolished and (b) polished polysilicon rotors at 0.5 meter distance from a grating microscanner using 633 nm laser. Note the increased intensity and reduced beam divergence as a result of polishing.

```
15-Mar-96
1:51:55
```

```
1
50 ms
200 mV
```

```
2
50 ms
200 mV
```

pkpk(1)	294 mV
mean(1)	91.6 mV
sdev(1)	104.2 mV
rms(1)	138.7 mV
ampl(1)	266 mV

```
50 ms
1 .2  V  DC
2 .2  V  DC
3 10 mV  DC        ⌐    1  DC 0.120 V
4 10 mV  DC
```

```
100 kS/s

□   AUTO
```

Figure 15. Typical scan intensity measured during the operation of the microscanner (#1). As a reference, a signal synchronous to excitation signal of the scanner micromotor is superimposed (#2).
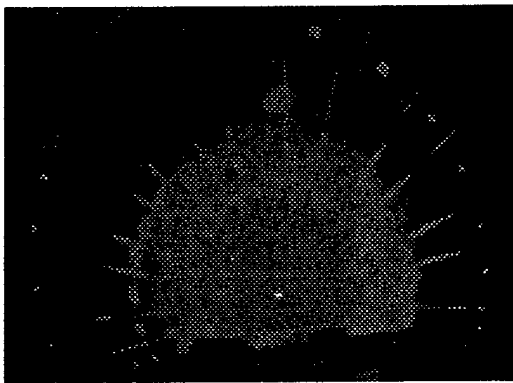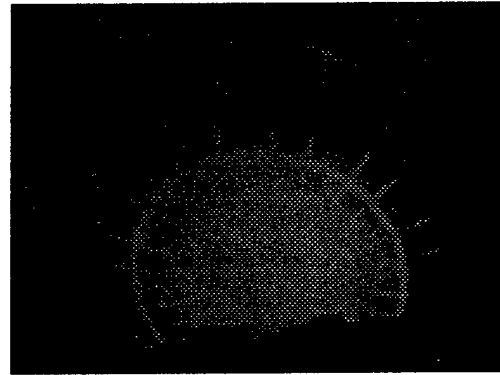
<div style="text-align:center">(a)   (b)</div>

Figure16. Typical scans obtained from microscanner operated in: (a) stepping; and (b) continuous modes.

Optical Rib Waveguides

Planar MOMS telecommunications chips will require optical waveguide fabrication technology which is compatible with the microfabrication technology used to produce lateral microstructures and microfabricated recesses. To this end, we have developed a silicon waveguide fabrication process which is compatible with our three-mask rapid prototyping and nickel plating processes. A waveguide technology which appears to meet all these requirements is that of a rib waveguide fabricated in epitaxial silicon [19]. The basic structure of a rib waveguide is shown below.
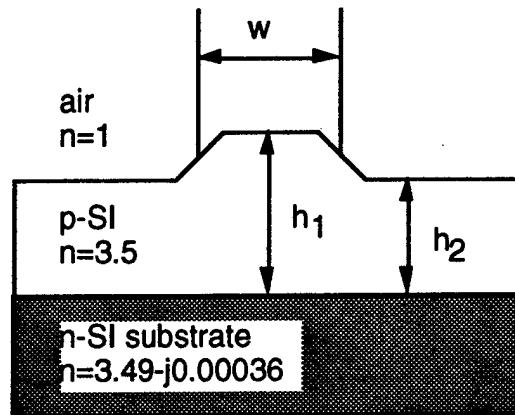
Figure 17. Cross-sectional view of a rib waveguide in epitaxial silicon.

We have fabricated all-silicon rib optical waveguides and U-groove alignment structures on (110) silicon substrates. Such all-silicon waveguides are compatible with our micromachining processing and are necessary components for MEMS based optical fiber devices. Rib waveguides consisting of 6.7 μm tall by 5-15 μm wide ribs have been RIE etched in lightly-doped epitaxial silicon layers deposited on heavily doped silicon substrates. Experimental measurements of these devices at 1550 nm indicates that the waveguides are single mode. The optical loss was measured to be as low as 1.68 dB/cm.

We have fabricated all silicon optical waveguides on (110) silicon wafers. A 20μm thick layer of epitaxial silicon with a doping level of less than 10^{15} cm^{-3} was deposited on 4" (110) silicon wafers having an n-type-phosphorous doping level of 10^{19} cm^{-3}. These wafers have a resistivity of 0.001 to 0.003 ohm-cm and an optical index of refraction of 3.49 at 1500 nm. . The epitaxial layer has a conductivity of 4.5 ohm-cm and a refractive index of 3.5 at 1500 nm. A 0.5μm masking film of thermal SiO_2 was grown on the substrate after the epitaxial deposition. The exposed silicon was then anisotropically etched in 17 wt. % KOH at 55° to produce long, narrow U-grooves in the silicon substrate for optical fiber alignment. The waveguide ribs are patterned and etched into the epitaxial silicon layer using Cl_2 reactive-ion-etching. Etching

depth was controlled to be 6.7µm by timed endpoint. The waveguides had nearly square rib profiles with a sidewall slope angle of approximately 83°. The sides of the rib structure were found to be visibly smooth when examined with a scanning electron microscope (SEM) indicating that the waveguides should not have excessive loss (a major obstacle to formation of low-loss waveguides is excess scattering due to rib surface roughness). Figure 18 shows the vertical rib profile obtained with Cl_2 RIE etching, and the high quality end-face obtained with ultrasonic KOH etching.
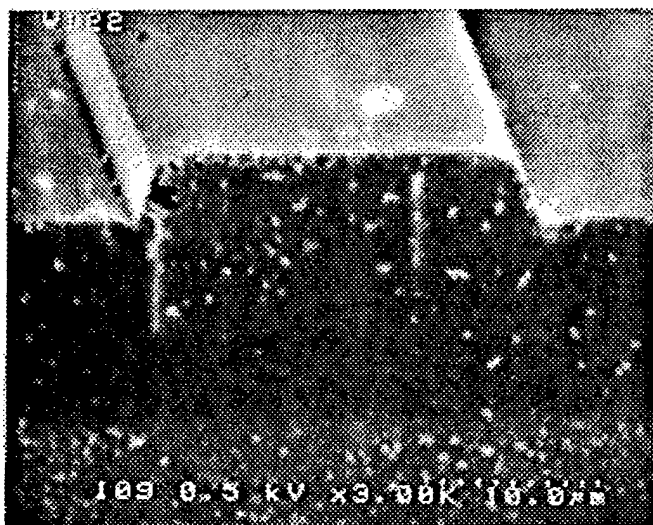

Figure 18. Anisotropically etched end-face of an all silicon waveguide. Note the darker gray of the epitaxial silicon and the lighter gray of the highly doped substrate caused by the conductivity difference between the silicon layers.

We have succeeded in producing single-mode, all-silicon waveguides with large, cross-sectional areas on (110) silicon (Figure 18). RIE etching was used to form the waveguide rib shapes in the epitaxial silicon. U-grooves are used for aligning optical fibers with the waveguides (Figures 19 and 20); standard vee grooves are not possible with this (110) orientation. After the patterning, an anisotropic KOH step was used to form the U-grooves for the placement of standard 125 µm core diameter optical fibers. The corner compensation structures seen in Figures 19 and 20 prevent the (111) crystal planes from entering the U-grooves where they would interfere with the fiber placement.
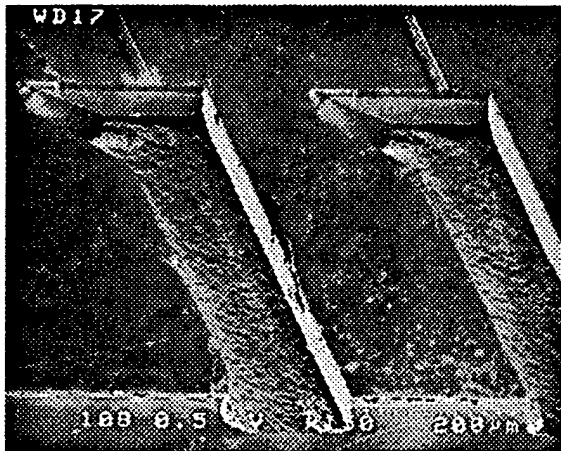
Figure 19. End view of bulk fabricated U-grooves. Note the rib waveguides positioned at the end of the grooves and the corner compensation structures.
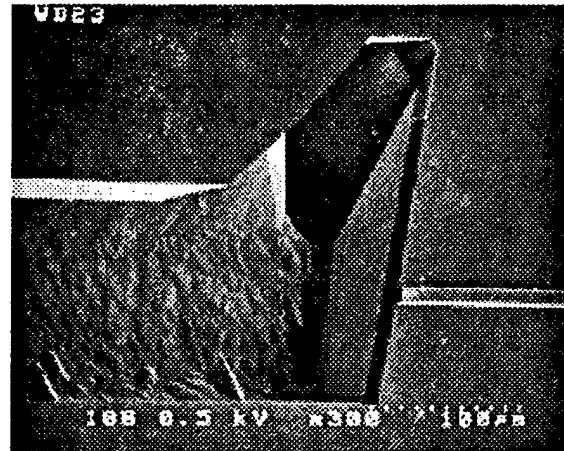
Figure 20. Detail of corner compensation structure of fiber guiding U-groove on a (110) silicon substrate. Note the rib waveguide at the right end of the U-groove.

Anisotropic etching of silicon for optical applications produced sidewalls which are less smooth than expected for the {111} planes [22]. Figure 21 demonstrates that the bottoms of U-grooves which are anisotropically etched in (110) silicon are not suitable for fiber optical applications. We found that etching a silicon substrate with a 70° C., 33% wt. percent KOH solution gave U-groove bottoms with a surface roughness of 5600Å. This amount of roughness is not suitable for positioning of fiber optical cables which have highly stringent alignment requirements. When ultrasonic agitation was applied with an identical etching solution, the surface roughness of the U-groove bottoms were reduced by a factor of 16 to a R_a of 340Å (Figure 22). The additional reduction of surface roughness with application of ultrasound is caused by breaking up bubbles which form in the U-grooves during the etching process.
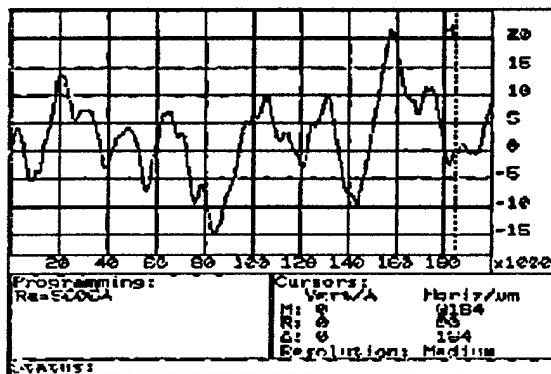

Figure 21. Decktak surface roughness of a typical U-groove bottom. Note that the value of R_a is 5606Å.
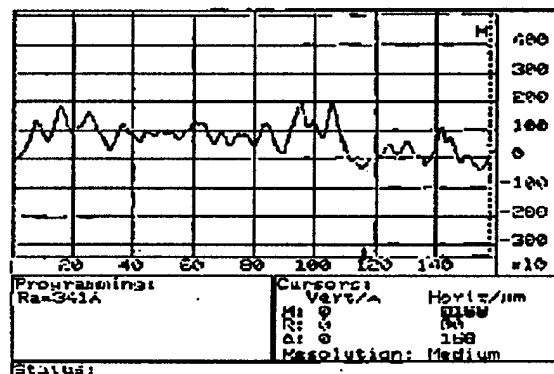
Figure 22. Decktak surface roughness of a U-groove bottom produced with ultrasonic etching. Note that the value of R_a is 341Å.

Controlling the depth variation to better than 1μm is not currently possible by the fabrication techniques available at CWRU, i.e. timed etch. The depth of the U-grooves is easily controlled to within 3 μm by careful timing of the etch, but the variation of etch depth across a wafer is at best 3μm.

The waveguide ribs and the 7000Å oxide masking layer stood up to 170 microns of etching without damage to the U-groove ribs. The slanting {111} plane is visible in the trench at this depth which verifies the need for the corner compensation structures as designed (Figures 23, 24). These structures prevent this plane from entering the U-groove trench for shallower etch depths.
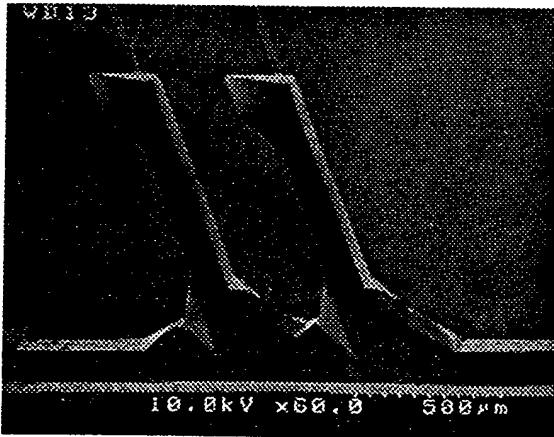

Figure 23. End view of bulk fabricated U-grooves using ultrasonic agitation. These grooves are visibly smoother than those shown in Figure 7. The rib waveguides are positioned at the end of the grooves.
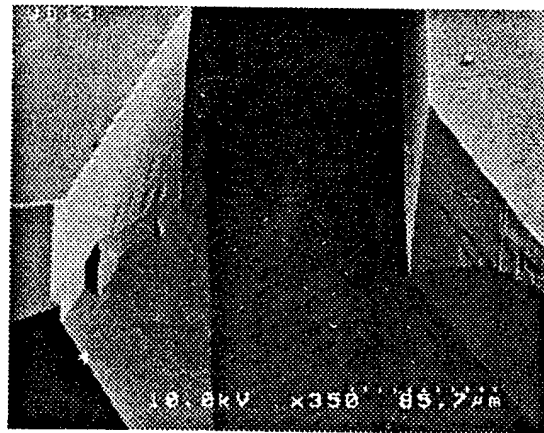

Figure 24. Detailed photo of the corner compensation mechanism required for U-grooves in (110) silicon. (Etched using ultrasonic agitation.)

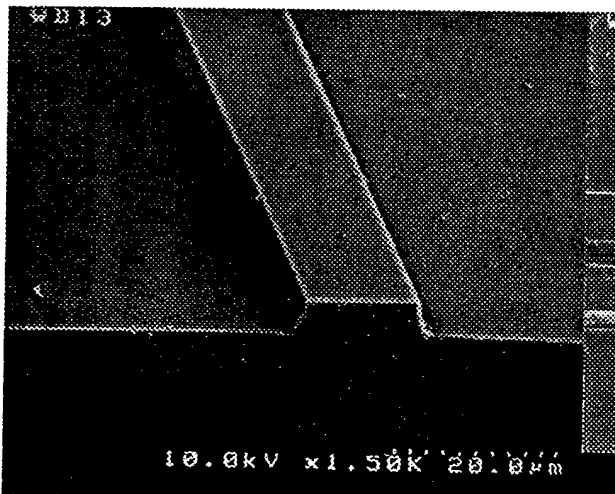Figure 25. Ultrasonically etched end-face of a rib waveguide with a rib height of 6.7μm, a base width of 15.5μm and an etch angle of 83.6°.
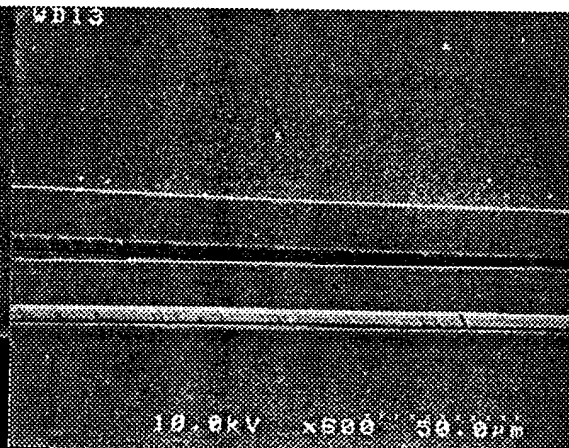

Figure 26. Top view of Y-coupler showing sharp definition of waveguide ribs using anisotropic etching with ultrasonic agitation.

These results show that the combination of bulk and surface micromachining are very feasible for fabrication of all-silicon waveguide ribs and bulk etched alignment structures. Figure 25 shows the very vertical rib profile 80-85° rib sidewalls are very smooth along the length of the waveguides when ultrasonic agitation is used. All-silicon waveguides are an attractive technology for development of MOMS systems. We have used bulk etching of (110) silicon with ultrasonic agitation to produce the directional coupler shown in Figure 26.

Optical characterization

A 1.5 µm laser diode source and an IR camera were used to determine three-dimensional beam profiles from straight waveguides with 6.7µm high by 10µm wide ribs. Figure 27(a) shows a far-field photograph of the output beam from such a waveguide and Figure 27(b) shows the corresponding three-dimensional profile of the beam's optical intensity. The beam is narrower in the vertical direction than in the horizontal direction due to the dimensions of the waveguide ribs and the epitaxial-layer thickness. These results are very promising for the all-silicon waveguide technology as single-mode optical waveguides are often system requirements.
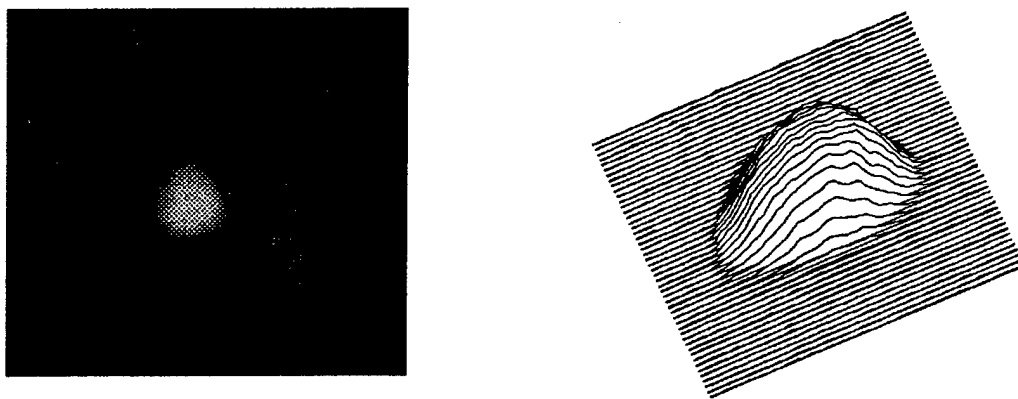

Figure 27. (a) Laser beam profile from a rib (b) Three-dimensional intensity profile.
waveguide with a 6.7µm tall rib

Waveguide loss measurements were comparable to the results obtained by Splett and Petermann [19] for (100) all silicon waveguides. Their best total loss measurement was given as 4.7 dB for waveguides with 15µm wide ribs. Their waveguides required end-face polishing because they were formed on (100) silicon wafers, while our waveguides with anisotropically etched end-faces do not require mechanical polishing to obtain results very similar to their polished waveguides. Since little difference in intensity results due to polarization variation was noted in the published literature, the polarization dependence of the devices was not investigated. Table 2 shows the results of loss measurements for our all-silicon waveguides.

Waveguide Width (µm)	Total Loss (dB)	Propagation Loss (dB/cm)
5	8.32	5.22
10	6.59	3.39
15	4.88	1.68

Table 2. Results of optical loss measurements from all-silicon optical waveguides. Propagation loss is estimated in a similar manner to the methods of Soref and Petermann [23], that is, subtracting 1.6 dB for Fresnel-loss and 1.6 dB of mode mismatch at the other end.

Laser Diode Tuner

A silicon micromachined micromirror and a laser diode have been successfully integrated. The micromirror forms an external cavity resonator for the laser diode and was fabricated by anisotropic etching of (110) silicon in conjunction with silicon-to-glass bonding. A mirror displacement of 1.43 μm and a corresponding wavelength variation of 30Å were attained.

A schematic diagram of an integrated laser diode and micromirror is shown in Fig. 28. The micromirror was fabricated by anisotropic etching of (110) silicon in conjunction with silicon-to-glass bonding [24]. Anisotropic etching of (110) silicon allowed the fabrication of a high-aspect ratio silicon plate with atomically smooth, vertical sidewalls because of the high etching selectivity between the (111) and (110) planes. This allowed the development of a cantilever beam actuator with lateral compliance. The electrodes located on the two sides of the cantilever beam provide the electrostatic force that deflects the beam; the (111) sidewall of the cantilever beam functions as the external mirror of an optical cavity including the laser diode bonded near the beam. Mechanical stoppers are located so that they limit the lateral deflection of the beam, preventing electrical shorting to the electrodes.
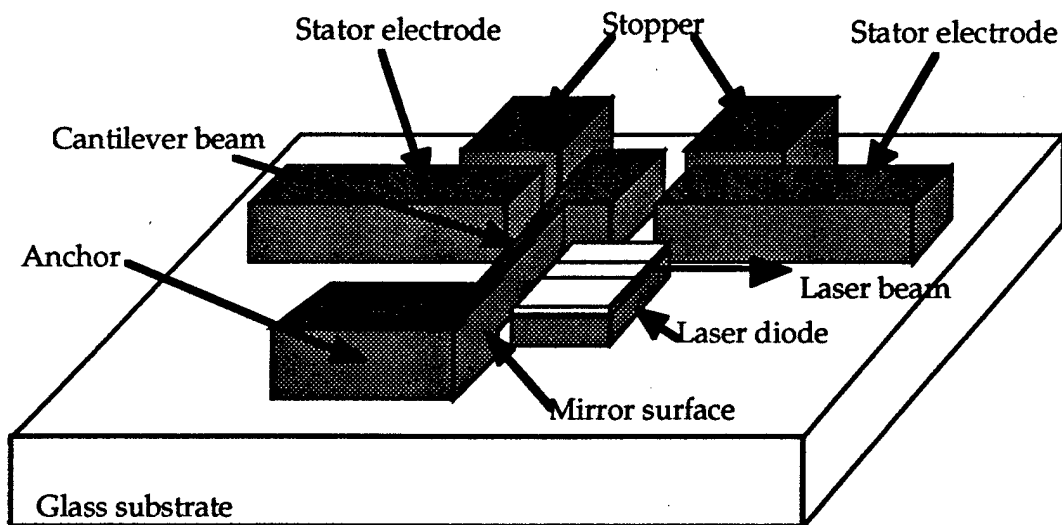
Figure 28. Schematic diagram of an integrated laser diode and micromirror.

Fabrication process
The fabrication process for the laser diode tuner is shown in Fig. 29. Shallow etching is performed, thereby separating the moving parts from the glass substrate in the final device. LPCVD silicon nitride is then deposited and patterned, defining the high-aspect-ratio features to be etched. Then, KOH anisotropic etching is performed to the desired depth. The (110) silicon wafer

is then electrostatically bonded to a Pyrex glass substrate. Next, the silicon wafer is polished from the back side until the structures are free to move. Finally the laser diode chip is bonded onto the substrate.

Si Shallow Etching by RIE

Si3N4

Silicon-Nitride Deposition

Anisotropic Deep Etching by KOH

Glass Substrate

Electrostatic Bonding

Cantilever beam   Anchor

Substrate Polishing Back
(to release the structure)

Laser Diode

Laser Diode chip Bonding
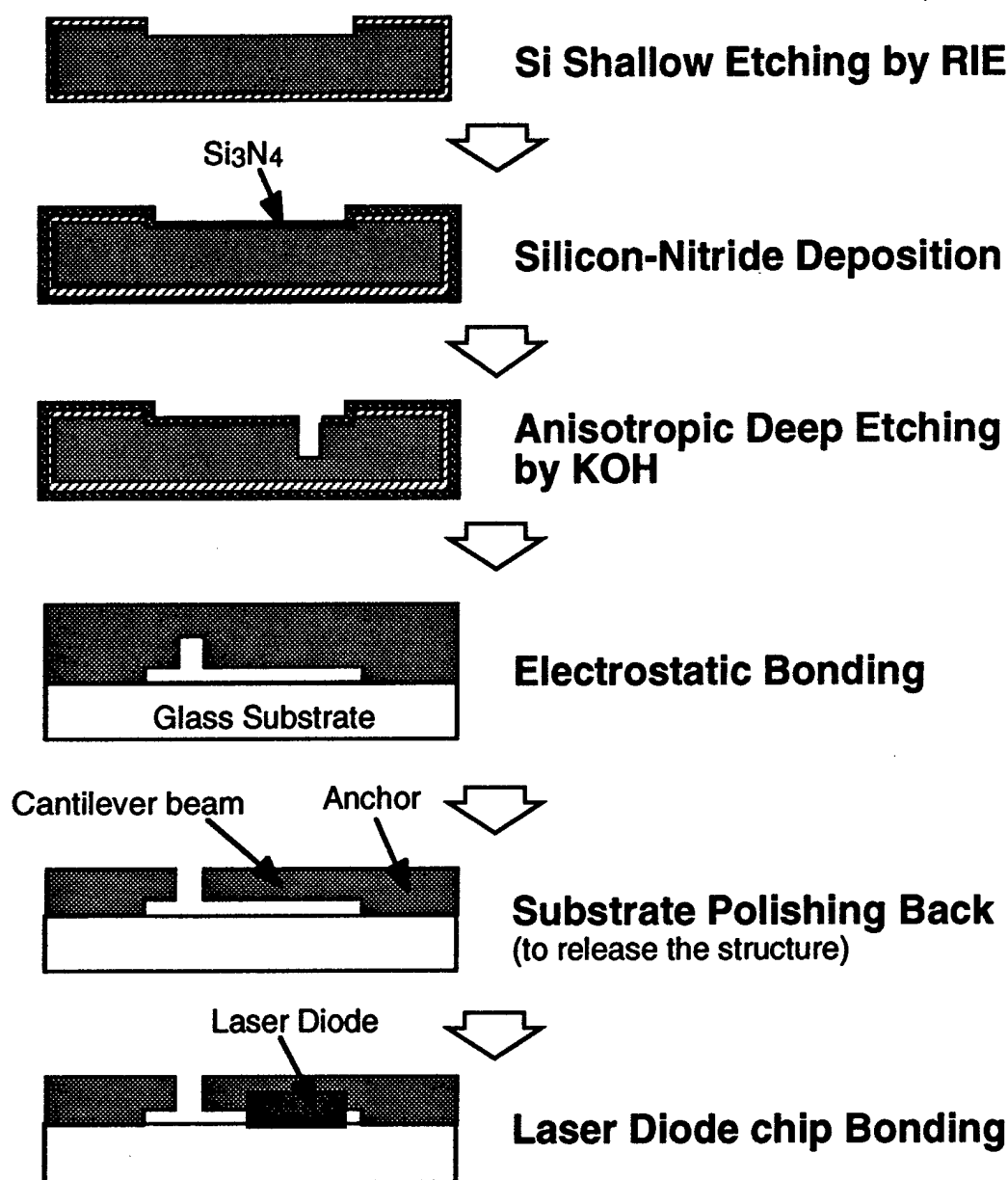
Figure 29. The fabrication process for the integrated LD and micromirror.

Figure 30 is an SEM image of the final device. The beam is about 1.7 mm long, 8 μm wide, and 130 μm high. The actuator gap between the beam and the stator electrode is 7 μm. The external cavity length, (the gap between the beam sidewall and the laser diode facet) is about 10 μm. The laser diode is a gain guide type with planar stripe; the active layer is an AlGaAs multiquantum

well structure. The cavity length of the laser diode is about 340 μm. The threshold current of laser diode without an external mirror is about 50 mA.
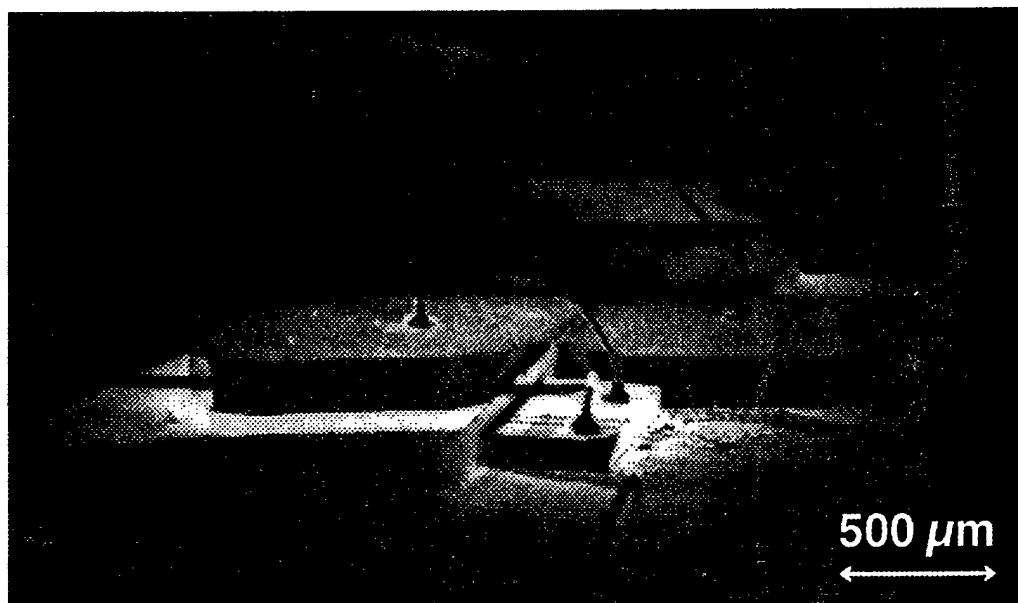
Figure 30. An SEM image of the integrated LD and micromirror.

Figure 31 shows the measured wavelength variation of the laser diode output as a function of the excitation voltage of the actuation mirror. The laser diode is operated using a 1-kHz, 0.2%-duty cycle current pulse to avoid raising the temperature of the laser diode. The wavelength shows discrete variation with a period of about 30Å. The discrete variation interval was 0.3 nm which coincides with the Fabry-Perot mode of the laser diode cavity length since there was no anti-reflection coating on the facet facing the mirror.

Figure 31. Wavelength variation as a function of the excitation voltage of the mirror.

Silicon Optical Etalon Fabrication Process [25]

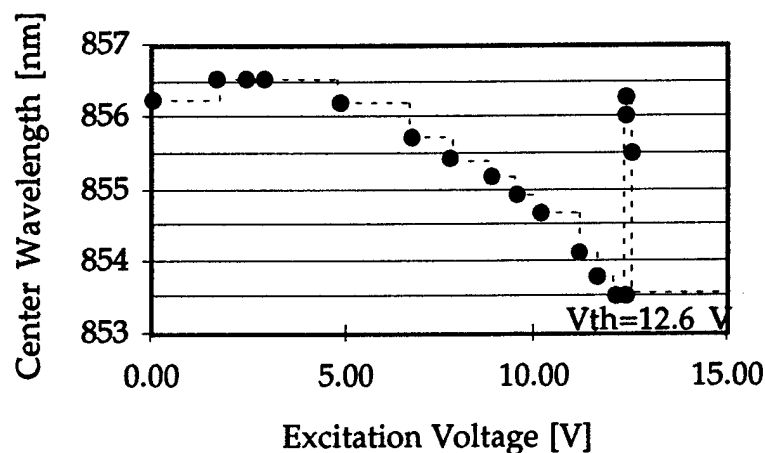Many optical devices require specialized optical coatings, for high reflectivity dielectric reflectors and for multi-layer anti-reflection coatings. Such "exotic" dielectric materials as zinc selenide and thorium fluoride are routinely used in the optics community, but have not been integrated into micromachined devices. Our approach to process integration is to do all microlithographic processing prior to any dielectric coating thereby keeping the processes separate and avoiding any contamination of the integrated circuit processing by the dielectric coatings. We used shadow masking to pattern the optical reflective coatings on a micromachined device DSP silicon wafer. We are constructing a tunable IR filter by bonding two DSP wafers with reflective dielectric coatings together to form an optical etalon. Mechanically, this requires maintaining strict tolerances on the spacing between the reflective coatings and the parallelism of the optical surfaces. Because of problems with maintaining the parallelism and controlling the spacing using conventional techniques we are exploiting the well-developed control of optical coating technology to our advantage. Specifically, we are using a KOH etched shadow mask to pattern precise thicknesses of the dielectric films used to produce the reflective coatings to act as the spacers between the two wafers. Additional depositions of the dielectric materials can be used to achieve the required spacing between the optical reflective coatings. We are currently investigating how to bond micromachined, optically coated surfaces together. The most attractive approach appears to be a patterned evaporative coating of a low melting point metal to act as a bonding layer.

We have also been developing tunable etalons for micromechanical modulators. The integration of multilayer dielectric optical coatings with microlithographic processing is required for micromechanical optical modulators and other devices. We have developed a process flow for producing tunable silicon IR etalons in the 1.4-6 μm wavelength region with dielectric coatings which avoids contaminating processing tools with the coating. These etalons (which we plan to use as optical modulators and filters) are constructed from two planar, parallel reflective surfaces separated by a distance d. The inner faces are coated with multilayer reflective coatings and the outer faces are coated with anti-reflection coatings. The support material for the optically reflective films is a standard double sided polished (DSP) silicon wafer. No additional surface polishing is necessary to insure good optical performance in the 1.4 to 6 micron wavelength region. Silicon substrates have a high and uniform transmittance for the near to mid infrared wavelengths from about 1.4 to 6 microns [26] which makes them very suitable for this particular application.

The reflective and antireflection coatings were not deposited completely across the wafer surface — they were patterned using a shadow mask

technique to pattern the silicon support material with the dielectric coatings. A silicon wafer with KOH etched openings was aligned to the device wafer and acted as a stencil, blocking the regions of the device wafer surface which are to be free from the reflective coating. Using standard 500 micron wafers as shadow masks resulted in approximately 0.5 mm of irregular deposition at the edges of the patterned coating. This does not pose a problem for large optical area devices.

The two reflective surfaces containing the thick, reflective coatings must be held parallel and apart by spacers. Since the top surfaces of the spacer layers are bonding/contact regions, they must be smooth. Additionally, the thickness must be uniform to ensure parallelism of the optical faces. Spacer layers were produced using the optical coating evaporative processes. The multilayer reflective coating was deposited on both optical and spacer regions through a shadow mask. A different shadow mask was then used to deposit additional layers onto the spacer regions to create the required gap between reflective surfaces.

We also investigated recessing one optical face within an etched cavity. The cavity is etched to the necessary depth determined by the reflective coating thickness and the plate separation to produce the required distance between the reflective coatings. A standard DSP wafer was thermally oxidized, photo-patterned, and oxide etched. A cavity was then etched into the silicon using KOH etching. KOH etching has two great drawbacks in this application. First, the cavity depth requires the etch be done without an etch stop yet etch depth is critical, so the process must be carefully timed. Second, KOH etched (100) planes are visibly rough and frequently pitted with irregularly spaced deep inverse pyramidal holes. This may not be significant for IR wavelength devices but becomes more critical as the wavelength decreases. Nevertheless, due to the processing advantages of a cavity etched spacer, we are currently working to develop a timed KOH etch with an acceptable surface roughness and planarity for these devices.

After the optical coating steps, the two wafers must be brought into contact and secured together. Alignment of the two wafers is accomplished through alignment holes etched through one wafer and corresponding fiducials on the other wafer. Shadow masks may be used to pattern an evaporative coating bonding layer on wafers that have already been coated with the reflective layers. The wafers may then be brought into contact, clamped and heated. We are investigating using low melting point metals as possible bonding agents [27, 28]. Work on this low-temperature bonding technique is in progress.

References:

1. K.Deng, M.Mehregany, and A.S.Dewa, "A Simple Fabrication Process for Side-Drive Micromotors," Technical Digest 7th International Confererence on Solid-State Sensors and Actuators (Yokohama, Japan, June 1993), p.756-759.

2. Y. Uenishi, M. Tsugai, and M. Mehregany, Micro-Opto-Mechanical Devices Fabricated by Anisotropic Etching of (110) Silicon, IEEE MEMS-94 Workshop, (Oiso Prince Hotel, Kanagawa, Japan, January 25-28, 1994).

3. S. Furukawa, S.Roy, H. Miyajima, Y. Uenishi and M. Mehregany, "Nickel Surface Micromachining, " Proceedings "Microstructures and Microfabricated Systems Symposium", at the 185th Electrochemical Society Meeting, San Francisco, California, May 22-27, 1994, pp. 38-46.

4. S. Roy and M. Mehregany, "Fabrication of Electrostatic Nickel Microrelays by Nickel Surface Micromachining," submitted to IEEE 1995 MEMS Workshop, Amsterdam, Netherlands.

5. H. Miyajima and M. Mehregany, "High-Aspect-Ratio Photolithography for MEMS Applications," submitted to J. Micromechanical Systems.

6. K.Deng, M.Mehregany, and A.S.Dewa, "A Simple Fabrication Process for Side-Drive Micromotors," Technical Digest 7th International Conference on Solid-State Sensors and Actuators (Yokohama, Japan, June 1993), p. 756-759.

7. H.Miyajima, K.Deng, M.Mehegany, F.L.Merat, and S.Furukawa, "Fabrication of polygon mirror microscanner by surface micromachining," Proceeding SPIE, Volume 2291, Integrated Optics and Microstructures II, 1994.]

8. S. Roy, S. Furukawa, H. Miyajima, and M. Mehregany, "In Situ Measurement of Young's Modulus and Residual Stress of Thin Electroless Nickel Films for MEMS Applications," presented at Materials Research Society Fall Meeting, Boston, MA, 1994.

9. S. Roy and M. Mehregany, "Fabrication of Electrostatic Nickel Microrelays by Nickel Surface Micromachining," submitted to IEEE 1995 MEMS Workshop, Amsterdam, Netherlands.

10. S. Roy, "Microfabricated Nickel Actuators by Surface Micromachining," M.S. Thesis, Case Western Reserve University, May 1995.

11. H.Miyajima, K.Deng, M.Mehegany, F.L.Merat, and S.Furukawa, "Fabrication of polygon mirror microscanner by surface micromachining," Proceeding SPIE, Volume 2291, Integrated Optics and Microstructures II, 1994.]

12. K. Deng, H. Miyajima, V.R Dhuler, M. Mehregany, S.W. Smith, F.L. Merat, and S. Furukawa, "The Development of Polysilicon Micromotors for Optical Scanner Applications" presented at 1994 Solid-State Sensor and Actuator Workshop," Hilton Head, South Carolina, June 1994.]

13. A.A. Yasseen, S.W. Smith, M. Mehregany and F.L. Merat, "Diffraction Grating Scanners Using Polysilicon Micromotors,"

14. T. Kamins, *Polycrystalline Silicon for Integrated Circuit Applications,* Kluwer Academic Publishers, Boston, 1988.

15. M.C. Hutley, *Diffraction Gratings,* Academic Press, London, 1982.

16. G.T. Mulhern, D.S. Soane, and R.T. Howe, "Supercritical carbon dioxide drying of microstructures," in *Technical Digest, 7th Int. Conf. on Solid-State Sensors and Actuators* (Yokohama, Japan, June 1993), pp. 296-299.

17. H. Kahn, S. Stemmer, K. Nandakurnar, A.H. Heuer, R.L. Mullen, R. Ballarini, and M.A. Huff, "Mechanical properties of thick, surface micromachined polysilicon films," in *Proceedings, IEEE Micro Electro Mechanical Systems* (San Diego, California, Feb. 1996), pp. 343-348.

18. K. Deng, R. Collins, M. Mehregany, and C. Sukenik, "Performance impact of monolayer coating of polysilicon micromotors," in *Proceedings, IEEE Micro Electro Mech~ Systems* (Amsterdam, the Netherlands, Feb. 1995), pp. 368-373.

19. A. Splett and K. Petermann, "Low Loss Single-Mode Optical Waveguides with Large Cross-Section in Standard Epitaxial Silicon," IEEE Photonics Technology Letters, Vol. 6, No. 3, March 1994, p. 425-427.

20. Richard A. Soref and Brian R. Bennett, "Electrooptical Effects in Silicon," IEEE J. of Quantum Electronics, Vol. QE-23, No. 1, January 1987, p. 123-187.

21. Y. Uenishi, M. Tsugai, and M. Mehregany, Micro-Opto-Mechanical Devices Fabricated by Anisotropic Etching of (110) Silicon, IEEE MEMS-94 Workshop, (Oiso Prince Hotel, Kanagawa, Japan, January 25-28, 1994).

22. K. Ohwada, Y. Negoro, Y. Konaka, and T. Oguchi , "Groove depth uniformization in (110) Si anisotropic etching by ultrasonic wave and and application to accelerometer fabrication," Proceedings of IEEE MEMS Workshop, Amsterdam, Netherlands, Jan. 1995, pp. 100-104.

23. Soref, J. Schmidtchen, and K. Petermann, "Large Single-Mode Rib Waveguides in GeSi-Si and Si-on-SiO_2," IEEE Photonics Technology Letters, Vol. 6, No. 3, pp. 1971-1974, Mar. 1994.

24. Y. Uenishi, M.Tsugai and M.Mehregany, "A hybrid-integrated laser-diode micro-external mirror fabricated by (110) silicon micromachining," submitted to IEE Electronics Letters.

25. James Klemic, J. Marcos Sirota, and Mehran Mehregany, "Fabrication Issues in micromachined tunable optical filters," SPIE Micromachining and Microfabrication '95, 23-24 October 1995, Austin, Texas.

26. R.D. Hudson, *Infrared System Engineering,* pp. 217-218, Wiley, New York, 1969.

27. Jan Haisma et al, Diversity and feasibility of direct bonding: a survey of dedicated optical technology," Applied Optics, Vol. 33, No. 7, pp. 1154-1169, March 1994.

28. Qin-Yi Tong et al, "Low temperature direct wafer bonding," *J. Micromechanical Systems,* Vol. 3, No. 1, pp. 29-35, March 1994.

Appendix 1

Micromotor Scanner Fabrication Process Traveler

Step	Process	Description
0	<000> n-type silicon wafers, resistivity: 1-25 Ω-m	
1	RCA Clean	Standard RCA clean
2	Deposit 4500 Å LPCVD Si_3N_4	Deposition done at BASC[1], measured thickness: 4527 Å
3	RCA Clean	Standard RCA clean
4	Deposit 3.5μm PSG	Deposition done at BASC, measured thickness: 35600 Å
5	Photo. anchor pattern definition, job file: SCAN1	Standard photo
6	BOE etch for Anchor definition	~5 min in doped BHF tank
7	Piranha strip the resist	Standard piranha clean ~iD the resist
8	RCA Clean	Standard RCA clean
9	Deposit 5μm LPCVD Polysilicon	Measured thickness: 5.5 μm[2]
10	RCA Clean	Standard RCA clean
11	Diffusion	Phosphorus, at 875°C for 7 hours Diffusion
12	PSG strip	BOE in doped tank, ~2min
13	CMP (in MEMS lab)	Base line recipe, 7-12min depending on initial film roughness
14	RCA clean (in MEMS lab)	Standard RCA clean
15	Piranha	Standard piranha clean
16	RCA clean	Standard RCA clean
17	Photo: grating pattern definition, job file: SCAN2	Resist coating at 6krpm
18	Grating etch	Lam standard SF_6-O_2 recipe for 1.5 min[3]
19	Piranha strip the resist	Standard piranha clean
20	Grow 0.5μm masking oxide at 900°C	Recipe: W9T5000, (time=250min)
21	Photo: rotor/stator pattern definition, job file: SCAN3	Standard photo
22	Rotor/stator masking oxide etch	Tegal, recipe C: optical endpoint
23	Rotor/stator pattern etch	Lam standard Cl_2 recipe, optical endpoint +15% overetch

24	Photo: flange mold pattern definition, job file: SCAN4	2 standard resist coats (coat, soft bake, coat), 200% overexposure[4]
25	BOE etch for flange mold definition	~10min in doped BHF tank
26	Piranha strip the resist	Standard piranha clean
27	RCA Clean	Standard RCA clean
28	Grow 0.5µm bearing clearance oxide at 900°C	Recipe: W9T5000, (time=250min)
29	RCA Clean	Standard RCA clean
30	Deposit 1µm LPCVD Polysilicon	Measured thickness: ~1.1µm
31	RCA Clean	Standard RCA clean
32	Diffusion	Phosphorus, at 875°C for 7 hours
33	PSG strip	BOE in doped tank, ~2min
34	Photo: bearing pattern definition, job file: SCAN5	2 standard resist coats (coat, soft bake, coat), 200% overexposure[4]
35	Bearing etch	Lam standard SF6-He recipe, optical endpoint +~200% overetch
36	Resist coating for front side protection	Coat and hard bake only
37	Backside etch 1µm of Polysilicon	Lam standard SF_6-He recipe, optical endpoint
38	BOE etch for backside bearing clearance oxide	~5 min in doped BHF tank
39	Backside etch 5µm of Polysilicon	Lam standard SF_6-He recipe, optical endpoint
40	BOE etch for backside PSG	~10min in doped BHF tank
41	Backside etch 4500A of Si_3N_4	Lam standard SF_6-He recipe, optical endpoint
42	Dice	Depth: ~200pm for mechanical rigidity, die size: ~1.4 x 1.4cm
43	Piranha strip the resist (in MEMS lab)	Standard piranha clean

[1] Berkeley Sensor and Actuator Center, University of California-Berkeley.

[2] Thickness was measured using Dektak after rotor/stator pattern etch.

[3] 1.5min results in ~5000A grating depth.

[4] Shorter or longer exposure times may be required depending on the age of the exposure lamp.

[5] Etch rate may change if the wafers undergo a longer or shorter thermal cycles prior to BOE (e.g., longer rotor/stator mask oxidation).

Appendix 2

Contract Related Publications

1. S.W. Smith, A.A. Yaseen, M. Mehregany, and F.L. Merat, Micromotor Grating Optical Switch, to appear in Optics Letters, August 1995.

2. F. Merat and M. Mehregany, "Integrated micro-opto-mechanical systems," presented at Photonics West '95 Miniaturized Systems with Micro-Optics and Micromechanics (M. Edward Motamedi) at Optoelectronics and Micro-Optical Devices Symposium SPIE Photonics West, February 1995, Proceedings SPIE, Vol. 2383, Miniaturized Systems with Micro-Optics and Micromechanics.

3. A.A. Yaseen, S.W. Smith, M. Mehregany, and F.L. Merat, "Diffraction Grating Scanners Using Polysilicon Micromotors," presented at IEEE 1995 MEMS Workshop, Amsterdam, Netherlands.

4. S. Roy, "Microfabricated Nickel Actuators by Surface Micromachining," M.S. Thesis, Case Western Reserve University, May 1995.

5. Y. Uenishi, M.Tsugai and M.Mehregany, "A hybrid-integrated laser-diode micro-external mirror fabricated by (110) silicon micromachining," submitted to IEE Electronics Letters.

6. S.W. Smith, A.A. Yaseen, M. Mehregany, and F.L. Merat, "Micromotor grating optical switch," Optics Letters, August 1995.

7. James Klemic, J. Marcos Sirota, and Mehran Mehregany, "Fabrication Issues in micromachined tunable optical filters," SPIE Micromachining and Microfabrication '95, 23-24 October 1995, Austin, Texas.

8. Steven W. Smith, Mehran Mehregany, Frank Merat, and David A. Smith, "All-silicon waveguides and bulk etched alignment structures on (110) silicon for integrated micro-opto-mechanical systems," presented at SPIE Photonics West, Micro Optics and Micro Structures III, Jan 29, 1996.

9. S.Smith, "Development of all-silicon waveguides and fiber guiding U-grooves," M.S. Thesis, Case Western Reserve University, January 1996.

10. F. Merat, "Micro-Opto-Mechanical Systems," American Vacuum Society MEMS Workshop, Anaheim, CA, September 28, 1995.

11. K. Deng, R. Collins, M. Mehregany, and C. Sukenik, "Performance impact of monolayer coating of polysilicon micromotors," in Proceedings, IEEE Micro Electro Mech~ Systems (Amsterdam, the Netherlands, Feb. 1995), pp. 368-373.

12. N.J. Mourlas, K.C. Stark, M. Mehregany, and S.M. Phillips, Exploring polysilicon micromotors for data storage micro disks,. in Proceedings, IEEE Micro Electro Mechanical Systems (San Diego, California, Feb. 1996), pp. 198-203.

13. S. Roy and M. Mehregany, "Fabrication of Electrostatic Nickel Microrelays by Nickel Surface Micromachining," IEEE 1995 MEMS Workshop, Amsterdam, Netherlands.

14. H. Miyajima and M. Mehregany, "High-Aspect-Ratio Photolithography for MEMS Applications," submitted to J. Micromechanical Systems.

15. A.A. Yasseen, S.W. Smith, M. Mehregany and F.L. Merat, "Diffraction Grating Scanners Using Polysilicon Micromotors," IEEE 1995 MEMS Workshop, Amsterdam, Netherlands.

16. S. Roy, S. Furukawa, H. Miyajima, and M. Mehregany, "In Situ Measurement of Young's Modulus and Residual Stress of Thin Electroless Nickel Films for MEMS Applications,"presented at Materials Research Society Fall Meeting, Boston, MA, 1994.